

Chip-Packaging Interaction and Reliability Impact on Cu/Low-k Interconnects

Xuefeng Zhang¹, Se Hyuk Im², Rui Huang², and Paul S. Ho¹

¹Microelectronics Research Center, ²Department of Aerospace Engineering and Engineering Mechanics, University of Texas, Austin, TX 78712

Abstract

1. Introduction

2. Experimental Techniques

2.1 Thermal deformation of plastic flip-chip package

2.2 Measurement of interfacial fracture toughness

3. Mechanics of Cohesive and Interfacial Fracture in Thin Films

3.1 Channel cracking

3.2 Interfacial delamination

4. Modeling of Chip-Packaging Interactions

4.1. Multilevel sub-modeling technique

4.2 Modified virtual crack closure (MVCC) method

4.3 Package level deformation

4.4 Energy release rate for stand-alone chips

5. Energy Release Rate under Chip-Package Interactions

5.1 Effect of low k dielectrics

5.2 Effect of solder materials and die attach process

5.3 Effect of low k material properties

6. Effect of Interconnect Scaling and Ultra Low k Integration

7. Summary

Acknowledgments

References

Chip-Packaging Interaction and Reliability Impact on Cu/Low-k Interconnects

Xuefeng Zhang¹, Se Hyuk Im², Rui Huang², and Paul S. Ho¹

¹Microelectronics Research Center, ²Department of Aerospace Engineering and Engineering Mechanics, University of Texas, Austin, TX 78712

Abstract

Chip-packaging interaction is becoming a critical reliability issue for Cu/low k chips during assembly into a plastic flip-chip package. In a flip-chip package, the thermal deformation of the package can be directly coupled into the Cu/low k interconnect structure inducing large driving forces for interfacial crack formation. This chapter summarizes the experimental and modeling studies to investigate the chip-package interaction and its impact on low k interconnect reliability. First, the packaging induced deformation and stress at the chip level is analyzed using high-resolution moiré interferometry and compared to thermal and process-induced stresses during chip fabrication. Then, results from 3D finite element analysis (FEA) based on a multilevel sub-modeling approach to investigate the chip-package interaction for low k interconnects is presented. Packaging induced crack driving forces for relevant interfaces in Cu/low k structures are deduced and compared with corresponding interfaces in Cu/TEOS structures. Effects due to the solder, underfill and low k material properties on packaging reliability are examined. Finally, the effects of interconnect scaling and multilevel

stacking on chip-package interaction and their impact on low k interconnect reliability is discussed.

1. Introduction

Continuous scaling has significantly improved the device density and performance of the Ultra Large Scale Integrated (ULSI) circuits. The exponential growth in device density has yielded high-performance microprocessor chips containing almost 1 billion transistors for the current 65nm technology [1]. The technology requires the implementation of new material, process and design for interconnect and packaging structures. Since 1997, copper (Cu) which has a lower resistivity than aluminum (Al) has been selected as an interconnect material to reduce the RC delay. At the 90 nm technology node, dielectric materials with k (dielectric constant) lower than silicon dioxide (SiO_2 , $k \sim 4$) were implemented into the Cu interconnects [2, 3]. As the technology advances, the interconnect structure continues to evolve with decreasing dimensions and increasing number of layers and complexity. At this time, the effort of the semiconductor industry is focused on implementing ultra-low k porous dielectric material ($k < 2.5$) into Cu interconnects to further reduce the RC delay. However, mechanical properties of the dielectric materials deteriorate with increase in the porosity raising serious concerns on the integration and reliability of Cu/low k interconnects.

For advanced ICs, the packaging technology is mainly based on the area-array

packages, or the flip-chip solder interconnects. This type of packages connects the active device side of the silicon die face-down via solder balls on a multilayered wiring substrate. The area-array configuration has the capability to support the I/O pad counts and power distribution required due to the improvement of the device density and performance. With the implementation of Cu/low k interconnects, the flip-chip package has also evolved including the implementation of plastic substrates with multilayered high-density wiring and solder balls with pitch reducing from hundreds of microns to tens of microns. The environmental safety mandates the change from Pb-based solders to Pb-free solders which are more prone to thermal cyclic fatigue failures and electromigration reliability problems [4, 5].

Structural integrity is a major reliability concern for Cu/low k chips during fabrication and when integrated into high-density flip-chip packages. The problem can be traced to the thermal deformation and stresses generated by the mismatch in thermal expansion between the silicon die with Cu/low k interconnects and the plastic substrate in the package [6]. Although the origin of the stresses in the interconnect and packaging structures is similar, the characteristics and the reliability impact for the low k interconnects are distinctly different. At the chip level, the interconnect structure when it is being built from the die surface is subjected to a series of thermal processing steps at each metal level including film deposition, patterning and annealing. The nature of the problem depends to a large degree on the thermal and chemical treatments used in the fabrication steps. For instance, for

deposition of metal and barrier layers, the temperature can reach 400°C and for chemical-mechanical polishing (CMP), the chip is under mechanical stresses and exposed to chemical slurries simultaneously. When subjected to such process-induced stresses, the low k interconnects due to the weak mechanical properties are prone to structural failure. Such mechanical reliability problems at the chip level have been extensively investigated [7].

When incorporated into the plastic flip-chip package, the fabrication of the silicon die containing the interconnect structure is already completed, so the interconnect structure as a whole is subjected to additional stresses coming from the packaging assembly process. Here the maximum temperature is reached during solder reflow for die attach. Depending on the solder materials, the reflow temperature is about 160°C for eutectic Pb alloys and about 250°C for Sn-based Pb-free solders. During accelerated or cyclic thermal tests, the temperature varies from 25°C to 125°C or 150°C. Although the assembly or test temperatures of the package are considerably lower than the chip processing temperatures, the chip configuration in the flip-chip package is different from that when it is stand-alone and very different stresses can exist in the low k interconnect structure. The thermal stress in the flip-chip package arises from the mismatch of the coefficients of thermal expansion (CTEs) between the chip and the substrate, which are 3 ppm/°C for Si and about 17 ppm/°C for a plastic substrate. The thermally induced shear stress on the solder balls reaches a maximum at the outermost solder row and increases with the size of the chip. By using underfills, the

shear stress at the solder bumps can be effectively reduced to improve package reliability [8]. However, the underfill causes the package to warp, resulting in large peeling stresses at the die-underfill and die-solder interfaces [9, 10]. The thermal deformation of the package can be directly coupled into the Cu/low k interconnect structure inducing large local stresses to drive interfacial crack formation. For a stand-alone die before packaging assembly, the energy release rate induced by a 400°C annealing is about 1 J/m^2 in Cu/ low k structures [11]. This is about 5x less than fracture energies measured for low k interfaces by 4-point bend tests [12, 13]. Nevertheless, interfacial delamination is commonly observed in low k interconnects after assembling the die into a flip-chip package. This has generated extensive interests recently to investigate chip-package interaction (CPI) and its reliability impact on Cu/low k structures [14-23].

In this chapter, we first review two experimental techniques important for the study of CPI and reliability. High-resolution moiré interferometry is a powerful experimental technique for measuring thermal deformation in a flip-chip package, whereas the mixed mode double cantilever beam test is capable of measuring the fracture energy for low k interfaces. This is followed by a general discussion of fracture mechanics in Section 3, including channel cracking and interfacial delamination in layered materials. Then, a three-dimensional (3D) multilevel sub-modeling method based on finite element analysis (FEA) is introduced in Section 4 to calculate the CPI induced energy release rates to drive interfacial delamination in

the low k interconnect structure. Such an approach is used in order to link the package deformation to the crack driving force in the interconnect structure where the feature dimensions differ at the chip and the package levels by several orders of magnitude. The modeling results are verified at the package level using thermal deformation measured by the high-resolution moiré interferometry. With a phase-shift technique, the resolution of moiré interferometry can reach 26 nm per fringe order, which is sufficient to determine deformation and strain distributions accurately within a small area, e.g. a solder bump in the package.

After verifying the model at the packaging level, multi-level sub-modeling is conducted one level of detail at a time, extending from the first sub-model level of the package around the solder bumps with the highest deformation to the final sub-model level of the Cu/low k interconnect. A modified virtual crack closure (MVCC) technique is used to calculate the energy release rate driving interfacial delamination by introducing a crack at relevant interfaces.

The chip-package interaction was found to depend on the thermal load during packaging assembly and the mechanical properties and dimensions of the dielectric and solder materials. In the die attach step, the maximum thermal load occurs during solder reflow before underfilling. With the high thermal load and without the underfill, the chip-package interaction is maximized and can become most detrimental to low k chip reliability. The maximum crack driving force is found to be at the outermost solder ball where the shear

stress in the low k structure is maximized. The discussion of the chip-package interaction in Sections 5 and 6 is first focused on the effects of dielectric and packaging materials including different low k dielectrics and Pb-based and Pb-free solders. Here the results are based on a two metal-level interconnect structure to simplify the modeling computation and to clarify the nature of the problem. The discussion is then extended in Section 6 to the study of the scaling effect where the reduction of the interconnect dimension is accompanied with more metal levels and the implementation of ultra-low k porous materials. A four metal-level interconnect structure is found to be sufficient to illustrate the effect of multilevel stacking and the elastic confinement on the crack driving force due to the combination of TEOS oxide or fully dense low k dielectric with ultra-low k dielectrics. Finally, some recent results on CPI induced crack propagation in the low interconnect and the use of crack-stop structures to improve the chip reliability are discussed.

2. Experimental Techniques

2.1 Thermal deformation of plastic flip-chip package

Thermal deformation of a flip-chip package can be determined using an optical technique of moiré interferometry. This is a whole-field optical interference technique with high resolution and high sensitivity for measuring the in-plane displacement and strain

distributions [24]. This method has been successfully used to measure the thermal-mechanical deformation in electronic packages to investigate package reliability [6, 9, 25]. In its standard form, a grating frequency of 1200 lines/mm is used, which yields a spacing of the interference fringe corresponding to 417 nm of in-plane displacement. The sensitivity is not sufficient, however, for measuring thermal deformation in high-density electronic packages, particularly for small features, such as solder bumps. For such measurements, a high-resolution moiré interferometry method based on the phase-shifting technique was developed, which measured the displacement field by precisely determining the phase angle of the two coherent incident beams. The phase angle is extracted as a function of position in the interferogram from four precisely phase-shifted moiré interference patterns [6, 10]. Once the phase angle is obtained, the continuous displacement s in the horizontal (u) and vertical (v) directions can be determined. The strain components can then be evaluated accordingly:

$$\varepsilon_x = \frac{\partial u}{\partial x}, \varepsilon_y = \frac{\partial v}{\partial y}, \gamma_{xy} = \frac{\partial u}{\partial y} + \frac{\partial v}{\partial x} \quad (2.1)$$

The high resolution moiré analysis was carried out for an experimental flip-chip package. The package was first sectioned and polished to reach the cross-section of interest. A schematic of the experimental flip-chip package with the cross-section that was analyzed is shown in Figure 2.1.

The moiré experiment was performed at room temperature (22°C) and the grating was attached to the cross-section of the specimen at the temperature of 102°C, providing a

reference (zero) deformation state and a thermal loading of -80°C [93]. An optical micrograph of the right half of the package cross-section is shown in Figure 2.2.

The displacement field (u and v) phase contour maps generated from the phase-shifting moiré interferometer with fringe spacing of 208 nm are shown in Figure 2.3. An outline of the interfaces obtained from the optical micrograph is superimposed onto the phase contour to highlight the local change of the displacement field in various packaging components. The global deformation of the u and v fields shows overall bending contours of the package due to warpage. This gives rise to the u field with relatively smooth horizontal (x) displacement distribution while the v field displays high density fringes in the solder bump-underfill layer, which is caused by the high CTE in this layer. The die corner at the right-bottom has the highest shear strain, which can be seen from the large displacement gradient along the vertical (y) direction in the u field.

The phase contours in Fig. 2.3 were used to map the displacement and strain distributions in the flip-chip package. The results are illustrated in Figure 2.4 where the displacement and strain distributions are determined along 3 lines: the silicon-solder interface (Line A), the centerline of solder bumps (Line B), and the centerline of the high density interconnect wiring layer above the BT substrate (Line C). Overall the normal strains ε_x and ε_y show the existence of a positive peeling stress in the bottom fillet area while the shear strain γ_{xy} reaches a maximum in the fillet of the underfill near the bottom die corner,

corresponding to the most critical stress concentration in the package. The strain components generally decrease toward the center of the packaging as expected and for the outermost solder balls, they can reach a value as high as 0.6% under a thermal load of -80°C. The strain induced by the package deformation is about 3 to 5 times larger than the thermal strain caused by thermal mismatch between the die and Cu/low k interconnect. It can be directly coupled into the low k interconnect structure near the outermost solder balls to drive crack formation. This underscores the importance of chip-package interaction in causing interfacial delamination in the interconnect structure, particularly with the incorporation of the low k dielectric with weak thermomechanical properties.

2.2 Measurement of interfacial fracture toughness

Fracture toughness (or critical energy release rate) is a key component for the reliability assessment of microelectronic devices. Measuring fracture toughness as a property of the material or interface is thus a critical procedure for materials characterization and selection for interconnects and packaging. Over the last twenty years, advances in fracture mechanics for thin films and layered materials [7, 26] have provided a solid foundation for the development of experimental techniques for the measurement of both cohesive and interfacial fracture toughness. In particular, the mechanics of channel cracking has been used in measuring cohesive fracture toughness of brittle thin films [27], which will be reviewed in

Section 3.1. Similarly, the mechanics of interfacial delamination has been widely used for interface toughness measurement. The basic mechanics of interfacial delamination will be reviewed in Section 3.2. This section discusses experimental techniques commonly used to measure fracture toughness of low k interfaces.

While a single-valued mode I toughness is typically sufficient for characterizing cohesive fracture in a homogeneous material (not for anisotropic materials or subcritical cracking), the interface toughness must be properly characterized as a function of the mode mix (see Section 3.2 for a definition). Consequently, different test structures and load conditions are often necessary for interface toughness measurements. A set of laminate fracture test structures were reviewed by Hutchinson and Suo [26] along with elasticity solutions for energy release rates and mode mix. A more recent review on interface toughness measurement techniques of thin-film structures was presented by Volinsky et al. [28].

Among many different measurement techniques, the double cantilever beam (DCB) [29] and four-point bend (FPB) techniques [30, 31] are most popular in microelectronics applications. In both techniques, one or more layers of thin film materials are sandwiched between two thick substrates (typically Si) so that the whole specimen is easy to load. Because the substrates are much thicker than the films, the energy release rate for an interfacial crack advancing between a film and a substrate or between two films can be calculated from the far-field loading on the substrates (i.e., the homogeneous solutions given

by Hutchinson and Suo [26]), neglecting the thin films. For the DCB test (Fig.2.5), the energy release rate under a symmetric loading (i.e., $F_1 = F_2 = P$) is given by

$$G = \frac{12(1-\nu^2)P^2a^2}{EB^2H^3}, \quad (2.2)$$

where E and ν are the Young's modulus and Poisson ratio of the substrate respectively, P is the applied force, a is the crack length, H is the substrate thickness, and B is the beam width.

With a pre-determined crack length, a critical load P_c to advance the crack can be determined from the load-displacement curve, and the interface toughness is then calculated by Eq. (2.2) as the critical energy release rate, i.e., $\Gamma = G(P_c)$. For the FPB test (Fig.2.6), the crack growth along the interface reaches a steady state with the energy release rate independent of the crack length

$$G = \frac{21(1-\nu^2)P^2L^2}{16EB^2H^3}, \quad (2.3)$$

where L is the distance between inner and outer loading points. The load P at the steady state can be determined from the plateau in the load-displacement diagram.

The mode mix for the sandwich specimen depends on the local conditions including the materials and thickness of the thin films. Using an arbitrary length scale l , the phase angle of mode mix as defined by Eq. (3.6) is related to the mode mix of the far field as [7]

$$\psi = \tan^{-1} \left(\frac{K_I^\infty}{K_{II}^\infty} \right) + \omega + \varepsilon \ln(l/h), \quad (2.4)$$

where K_I^∞ and K_{II}^∞ are the stress intensity factors from the homogeneous far-field solution, ω is an angle depending on the elastic mismatch between the films and substrates,

and h is the thickness of one of the films. For the case of a single film between two substrates, Suo and Hutchinson [32] found that ω is less than 10° provided that the elastic mismatch is not too large. It is rather cumbersome to calculate ω when several films are sandwiched. A common practice has been to specify the mode mix for the sandwich specimens by the far-field phase angle, $\psi_\infty = \tan^{-1}(K_{II}^\infty / K_I^\infty)$. For the symmetric DCB test, $\psi_\infty = 0$, i.e., a nominally mode I far field. For the FPB test, $\psi_\infty \approx 41^\circ$. Other mode mix can be obtained by using generalized laminated beam specimens loaded under cracked lap shear (mixed mode) or end-notched flexure (mode II) conditions [33] or by a modified DCB test configuration as described below.

An instrument to measure interfacial fracture energy under arbitrarily mix-mode loading was developed using the approach originally conceived by Fernlund and Spelt [34]. This instrument utilizes a double cantilever beam (DCB) sample, with a loading fixture as illustrated in Figure 2.7. By changing the positions of the different links in the link-arm structure, the forces, F_1 and F_2 , applied respectively on the upper and lower beams, can be changed to adjust the mode mix. The instrument allows interfacial fracture measurements for phase angles ranging from 0° (pure tension, $F_1 = F_2$) to 90° (pure shear, $F_1 = -F_2$). Additionally, multiple tests can be run on the same sample. The challenge of this technique resides in the crack length measurement, which is required for deducing the fracture energy for the DCB configuration. The energy release rate per unit crack length can be calculated as

$$G = \frac{6(1-\nu^2)F_1^2a^2}{EB^2H^3} \left[1 + \left(\frac{F_2}{F_1} \right)^2 - \frac{1}{8} \left(1 - \frac{F_2}{F_1} \right)^2 \right]. \quad (2.5)$$

The phase angle varies as a function of the ratio F_1/F_2 :

$$\psi = \arctan \left[\frac{\sqrt{3}}{2} \frac{\left(\frac{F_1}{F_2} - 1 \right)}{\left(\frac{F_1}{F_2} + 1 \right)} \right]. \quad (2.6)$$

This mixed-mode DCB test can measure the interface toughness as a function of the phase angle (from 0° to 90°), as shown in Figure 2.8 for a porous low k ($k \sim 1.9$) thin film structure. The measured interface toughness in general exhibits a trend to increase as the phase angle increases. It is understood that the shearing mode promotes inelastic deformation in the constituent materials and near-tip interface contact/sliding, both contributing to the energy dissipated as the crack advances. An overview of various mechanisms responsible for the strong dependence of interface toughness on the mode mix was given by Evans et al. [35] and more recently by Lane [36]. Experimentally, Dauskardt et al. [31, 37] have shown that the interface toughness between two elastic layers measured from the FPB tests decreases as the thickness of an adjacent ductile layer decreases. Several scenarios where plasticity affects the measurement of interface toughness in thin film structures were discussed by Suo [7]. There exist two limiting behavior: when the ductile layer is very thick, the plastic zone is fully developed as the crack advances, and the measured toughness is independent of the film thickness; when the ductile layer is very thin, the dislocation motion responsible for the plastic deformation is strongly confined, and the measured toughness approaches the intrinsic

work of adhesion. A variety of theoretical and numerical models have been developed to study the effects of plasticity on interface fracture. Among them, the embedded process zone (EPZ) model with cohesive interfaces [38] appears to be most versatile and relatively straightforward for numerical implementations.

The measurements of interface fracture toughness provide a tool for materials selection and process control in microelectronics industry. One typically measures the fracture toughness for specific interfaces under various process conditions, and then selects the material and condition that gives an adequate toughness. In the development of Cu interconnects, new barrier layers were required to prevent copper diffusion into dielectrics, and to provide adhesion of copper to the dielectrics. Using the FPB technique, Lane et al. [39] measured the interface toughness and subcritical cracking for a range of Ta and TaN barrier layers, and showed that the presence of N significantly improves the adhesion and resistance to subcritical cracking. Moreover, a cap layer is typically used to suppress mass transport and thus improve electromigration (EM) reliability of the Cu interconnects. A correlation between the EM lifetime and interface toughness was demonstrated so that the interface toughness measurements can be used as a screening process to select cap layer materials and processes [40, 41]. Sufficient interface toughness is also a requirement for the integration of low k dielectric materials in interconnect structures. Recently, the FPB technique has been adapted to quantitatively determine the effective toughness of different

designs of crack stop structures to prevent dicing flaws at the edge of chips from propagating into the active areas under the influence of thermal stresses during packaging [42].

3. Mechanics of Cohesive and Interfacial Fracture in Thin Films

Integration of low-k and ultralow-k dielectrics in advanced interconnects has posed significant challenges for reliability issues due to compromised mechanical properties. Two types of failure modes have been commonly observed: cohesive fracture of the dielectrics [43-45] and interfacial delamination [46, 47]. The former pertains to the brittleness of low-k materials, and the latter manifests as a result of poor adhesion between low k and surrounding materials. This section briefly reviews the mechanics underlying fracture and delamination in thin films with applications for integrated Cu/low k interconnects.

In an idealized thin-film structure with an elastic film on an elastic substrate, the mismatch in the elastic properties between the film and the substrate plays a critical role in the mechanical behavior and can be described by using two Dundurs' parameters [26]

$$\alpha = \frac{\bar{E}_f - \bar{E}_s}{\bar{E}_f + \bar{E}_s} \quad \text{and} \quad \beta = \frac{\bar{E}_f(1-\nu_f)(1-2\nu_s) - \bar{E}_s(1-\nu_s)(1-2\nu_f)}{2(1-\nu_f)(1-\nu_s)(\bar{E}_f + \bar{E}_s)}, \quad (3.1)$$

where $\bar{E} = E/(1-\nu^2)$ is the plane-strain modulus and ν is Poisson's ratio, with the subscripts f and s for the film and substrate, respectively. When the film and the substrate have identical elastic moduli, we have $\alpha = \beta = 0$, while $\alpha > 0$ for a stiff film on a

relatively compliant substrate and $\alpha < 0$ for a compliant film on a relatively stiff substrate.

The role of β is often considered secondary compared to that of α , sometimes ignored for simplicity.

3.1 Channel cracking

A tensile stress in an elastic film can cause cohesive fracture by channel cracking. Unlike a freestanding sheet, fracture of the film bonded to a substrate is constrained (assuming no delamination for the time being). As a result, the crack arrests at a certain depth from the film surface (often at or close to the film/substrate interface) and propagates in a direction parallel to the surface, forming a “channel crack” as illustrated in Fig. 3.1. Fig. 3.2a shows an array of parallel channel cracks, and Fig. 3.2b shows the cross section in the wake of a channel crack [48]. A systematic study on the mechanics of channel cracking in thin films was carried out by Beuth [49], and the main results were summarized in Hutchinson and Suo [26].

For an elastic thin film bonded to an elastic substrate, the energy release rate for steady-state growth of a channel crack takes form

$$G_{ss} = Z(\alpha, \beta) \frac{\sigma_f^2 h_f}{\bar{E}_f}, \quad (3.2)$$

where σ_f is the tensile stress in the film, h_f is the film thickness, and the dimensionless

coefficient Z depends on the elastic mismatch between the film and the substrate. At the steady state, the crack opening far behind the channel front does not change as the channel advances. Therefore, the energy release rate is independent of the channel length. Using a two-dimensional (2D) model [50], one can calculate the crack opening displacement, $\delta(z)$, from which the energy release rate for channel cracking can be determined, namely

$$G_{ss} = \frac{\sigma_f}{2h_f} \int_0^{h_f} \delta(z) dz . \quad (3.3)$$

By comparing Eqs. (3.2) and (3.3), the coefficient Z can be determined. The value of Z represents the constraint effect on channel cracking due to the substrate, which is plotted in Fig.3.3 as a function of α . When the film and the substrate have identical elastic moduli, $Z = 1.976$. It decreases slightly for a compliant film on a relatively stiff substrate ($\alpha < 0$). A compliant substrate ($\alpha > 0$), on the other hand, provides less constraint, and Z increases. For very compliant substrates (e.g., organic low k dielectrics), Z increases rapidly, with $Z > 30$ for $\alpha > 0.99$.

While the 2D model is sufficient to determine the driving force (energy release rate) for the steady-state growth of channel cracks, a three-dimensional analysis showed that the steady state is reached when the length of a channel crack exceeds two to three times the film thickness [51]. When the substrate material is more compliant than the film, however, the crack length to achieve the steady state can be significantly longer [52]. With all the subtleties

aside, the steady-state energy release rate for channel cracking offers a robust measure for the reliability of thin-film structures, which has also been used for experimental measurements of cohesive fracture toughness of dielectric thin films [27] and crack driving forces in integrated low k interconnects [48].

Recently, channel cracking in more complex integrated structures with low k materials has been investigated, such as multilevel patterned film structures [44] and stacked buffer layers [45]. It was found that the driving force for the growth of channel cracks in an embedded layer (also called *tunneling cracks*) is significantly reduced. Therefore, adding a tough cap layer on top of the film can enhance the constraint effect and thus suppress cracking in the film.

In addition to the elastic constraint, the roles of interface debonding, substrate cracking, and substrate plasticity have been studied. As shown by Tsui et al. [45], while a brittle film cracks with no delamination on a stiff substrate, interfacial delamination was observed when the film lies on a more compliant buffer layer. The driving force for channel cracking with interfacial delamination can be significantly higher than that with no delamination [53, 54]. Ye et al. [53] have shown that the driving force for channel cracking increases if the crack can penetrate into the substrate. Similarly, when the substrate deforms plastically, the constraint on film cracking is reduced. The effect of plastic deformation in ductile substrates on channel cracking has been studied by using a shear-lag model [55] and

finite element methods [52, 56]. Furthermore, the constraint effect can be completely lost over time if the substrate creeps [57, 58], leading to higher energy release rates.

When the steady state energy release rate of channel cracking reaches or exceeds the cohesive fracture toughness of the film, fast crack growth in the film is expected. In the subcritical regime ($G < G_c$), however, slow growth of channel cracks in thin films may be facilitated by environmental effects or thermal cycles. The consequence of slow crack growth can be critical for long term reliability and lifetime of devices. Several mechanisms for the slow growth of channel cracks in thin films have been studied, including environmentally assisted cracking [43,45], creep-modulated cracking [57-60], and ratcheting-induced cracking [61, 62]. For the environmentally assisted cracking, the transport of environmental molecules, such as water, and the chemical reaction at the crack front set the time scale that determines the crack velocity. For a given environment, a relationship between the crack velocity (V) and the crack driving force (energy release rate, G) can be measured experimentally. The measured crack velocity can also be used to infer the fracture driving force as well as other material properties in more complex integrated structures [48]. Alternatively, if the film is bonded to a viscous substrate or underlayer, the channel crack growth is modulated by the viscous flow or creep. For a linearly viscous underlayer, a steady-state velocity was predicted, which is inversely proportional to the underlayer viscosity and the film toughness [59]. This provides a means to determining viscosity by measuring the crack velocity.

Coupling of the creep-modulated cracking and environmentally assisted cracking leads to a steady state with a particular crack velocity and driving force at the intersection of the two V-G curves, as illustrated in Fig. 3.4. More general time-dependent behavior of channel cracks in integrated structures with viscoelastic [58] and power-law creep [60] materials has also been studied. Another interesting crack growth mechanism in thin films is due to ratcheting of elastic-plastic underlayers subjected to thermal cycling [61, 62]. In this case, ratcheting of the ductile underlayer due to accumulation of plastic deformation over temperature cycles builds up the stress in a brittle film atop, eventually leading to fracture of the brittle film. An analogy between ratcheting and creep has been established to understand the stress evolution during thermal cycles and to evaluate various design options to alleviate film cracking [62].

3.2 Interfacial delamination

Integration of diverse materials relies on interfacial integrity. Typically, an interfacial crack nucleates from a site of stress concentration such as a free edge of the film, a geometric or material junction in a patterned structure. Under tension, a channel crack in a film may lead to delamination from the root of the channel [54]. Under compression, buckling of the film can drive propagation of delamination, leading to coupled buckle-delamination blisters (e.g., telephone cord blisters) [26].

Due to asymmetry in the elastic moduli with respect to a bi-material interface,

propagation of an interfacial crack is in general under a mixed mode condition, as opposed to the pure mode I path in a homogeneous, isotropic solid. As a result, the fracture toughness of an interface is necessarily expressed as a function of the mode mix. However, the stress field around an interfacial crack tip in general cannot be decoupled into pure mode I and mode II fields, due to the oscillatory singularity at the crack tip. The stress field near an interfacial crack tip was first obtained by Williams [63]. A unified general description was given by Rice [64], which was adopted by Hutchinson and Suo [26] in particular for thin films and layered materials. For a two-dimensional interfacial crack between two isotropic elastic solids joined along the x -axis as illustrated in Fig. 3.5, the normal and shear tractions on the interface directly ahead of the crack tip are given by

$$\sigma_{yy} = \frac{K_1 \cos(\varepsilon \ln r) - K_2 \sin(\varepsilon \ln r)}{\sqrt{2\pi r}}, \quad \sigma_{xy} = \frac{K_1 \sin(\varepsilon \ln r) + K_2 \cos(\varepsilon \ln r)}{\sqrt{2\pi r}}, \quad (3.4)$$

where r is the distance from the crack tip, and ε is the index of oscillatory singularity depending on the second Dundar's parameter

$$\varepsilon = \frac{1}{2\pi} \ln \left(\frac{1-\beta}{1+\beta} \right). \quad (3.5)$$

The stress intensity factors, K_1 and K_2 , are the real and imaginary parts of the complex interfacial stress intensity factor, $K = K_1 + iK_2$.

When $\varepsilon = 0$, the interfacial crack tip stress field reduces to the homogeneous crack tip field with tractions, $\sigma_{yy} = \frac{K_1}{\sqrt{2\pi r}}$ and $\sigma_{xy} = \frac{K_2}{\sqrt{2\pi r}}$, where K_1 and K_2 are the conventional mode I and mode II stress intensity factors. In this case, the ratio of the shear traction to the

normal traction is simply K_2/K_1 , which defines the mode mix. When $\varepsilon \neq 0$, however, the mode mix as a measure of the proportion of “mode 2” to “mode 1” requires specification of some length quantity since the ratio of the shear traction to the normal traction varies with the distance to the crack tip. As suggested by Rice [64], an arbitrary length scale (l) may be used to define a phase angle of the mode mix for interfacial delamination, namely

$$\psi = \tan^{-1} \left[\left(\frac{\sigma_{xy}}{\sigma_{yy}} \right)_{x=l} \right] = \tan^{-1} \left[\frac{\text{Im}(Kl^{ie})}{\text{Re}(Kl^{ie})} \right]. \quad (3.6)$$

The choice of the length l can be based on the specimen geometry, such as the film thickness, or based on a material length scale, such as the plastic zone size at the crack tip. Different choices would lead to different phase angles. A simple transformation rule was noted by Rice [64] that transforms the phase angle defined by one length scale to another, namely,

$$\psi_2 = \psi_1 + \varepsilon \ln(l_2/l_1), \quad (3.7)$$

where ψ_1 and ψ_2 are the phase angles associated with lengths l_1 and l_2 , respectively. Therefore, so long as a length scale is clearly presented for the definition of the phase angle, experimental data for the mode-dependent interface toughness can be unambiguously interpreted for general applications, i.e., $\Gamma(\psi_1, l_1) = \Gamma(\psi_2, l_2)$.

The energy release rate for crack advancing along an interface is related to the interfacial stress intensity factors by [26]

$$G = \frac{1-\beta^2}{E^*} (K_1^2 + K_2^2), \quad (3.8)$$

where $E^* = 2(\bar{E}_1^{-1} + \bar{E}_2^{-1})^{-1}$. The criterion for interfacial delamination can then be stated as:

$G = \Gamma(\psi, l)$, where the same choice of the length l has to be used in the definition of the phase angle for the interface toughness and in the calculation of the phase angle for the specific problem along with the energy release rate G . For 3D problems, a mode III term must be added into the energy release rate, and another phase angle may be defined for the 3D mode mix.

For delamination of an elastic thin film from a thick elastic substrate under the plane-strain condition, it reaches a steady state when the interfacial crack length is much greater than the film thickness. The energy release rate for the steady-state delamination is independent of the crack length:

$$G_{ss}^d = \frac{\sigma_f^2 h_f}{2\bar{E}_f}. \quad (3.9)$$

Taking the film thickness as the length scale ($l = h_f$), the phase angle of mode mix at the steady state depends on the elastic mismatch as a function of the Dundar's parameters, i.e., $\psi_{ss} = \omega(\alpha, \beta)$. This function was determined numerically using an integral equation method and the computed values were tabulated by Suo and Hutchinson [65]. When the film and the substrate have identical elastic moduli, $\psi_{ss} = \omega(0,0) = 52.1^\circ$.

Yu et al. [66] have shown that the energy release rate for an interfacial crack

emanating from a free edge can be significantly lower than the steady-state energy release rate. Consequently, there exists a barrier for the onset of delamination, which depends on the materials and geometry near the edge. For a film whose edge lies on a flat substrate surface extending far beyond the edge, the energy release rate of interfacial delamination approaches the steady-state value very fast, suggesting a very small barrier for this case. On the other hand, for a film whose edge aligns with the edge of the substrate, the energy release rate has a slow approach to the steady-state limit as the crack length increases, suggesting a substantial barrier to initiation of delamination in this case. The elastic mismatch between the film and the substrate has a quantitative influence on how fast the energy release rate approaches the steady state. The mode mix however was found to reach the steady state value at a much shorter crack length.

For interfacial delamination from the root of a channel crack [53, 54], the energy release rate approaches the same steady state value, but follows a power law at the short crack limit [67],

$$G_d \sim \left(\frac{d}{h_f} \right)^{1-2\lambda}, \quad (3.10)$$

where d is the crack length, and λ depends on the elastic mismatch determined by the equation

$$\cos \lambda \pi = \frac{2(\beta - \alpha)}{1 + \beta} (1 - \lambda)^2 + \frac{\alpha + \beta^2}{1 - \beta^2}. \quad (3.11)$$

As shown in Fig. 3.6, the energy release rate approaches zero as $d/h_f \rightarrow 0$ when $\alpha < 0$

(compliant film on stiff substrate). Thus there exists a barrier for the onset of delamination.

On the other hand, when $\alpha > 0$ (stiff film on compliant substrate), the energy release rate approaches infinity as $d/h_f \rightarrow 0$, suggesting that interfacial delamination always occurs concomitantly with channel cracking. In Cu/low k interconnects, the low-k dielectrics is usually more compliant compared to the surrounding materials. Therefore, channel cracking of low-k dielectrics is typically not accompanied by interfacial delamination. However, when a more compliant buffer layer is added adjacent to the low-k film, interfacial delamination can occur concomitantly with channel cracking of the low-k film [45]. Moreover, a relatively stiff cap layer (e.g., SiN) is often deposited on top of the low-k film. Channel cracking of the cap layer on low-k could be significantly enhanced by interfacial delamination.

For a delamination crack with a circular front, for example, emanating from the edge of a circular hole, the energy release rate is

$$G = \frac{\sigma_f^2 h_f}{2\bar{E}_f} \frac{4}{[(1+\nu_f)+(1-\nu_f)(b/b_0)^2]}, \quad (3.12)$$

where b_0 is the radius of the circular edge and b is the radius of the circular delamination front. Note that there is no steady state for circular delamination. Instead, the energy release rate for the circular delamination monotonically decreases as the delamination zone expands.

A critical radius at which the delamination crack arrests can be determined by equalizing the energy release rate to the interface toughness. The phase angle of mode mix is independent of

b/b_0 when $(b-b_0)/h$ is sufficiently large, and is identical to the plane-strain solution. The stable circular delamination has been used to measure interface toughness for coatings and thin films [68, 69].

Energy release rate and mode mix of interfacial delamination in more complex integrated structures are commonly calculated for device reliability analysis. Here, finite element based models are typically constructed to compute stress intensity factors or energy release rates of interfacial cracks literally introduced in the model. Nied [70] presented a review focusing on applications in electronic packaging. Liu et al. [46] analyzed delamination in patterned interconnect structures. As one of emerging reliability concerns for advanced interconnects and packaging technology, impacts of chip-package interactions on interfacial delamination have been investigated by multi-level finite element models, which will be discussed in the next section.

The experimental techniques to measure interface toughness as the critical energy release rate ($\Gamma = G_c$) for fast fracture have been discussed in Section 2.2. In addition, interfacial cracks are often susceptible to environmentally assisted subcritical growth [29-31, 36, 71, 72]. Analogous to channel cracking of brittle thin films, the growth rate of an interfacial crack can be measured as a function of the energy release rate in the subcritical regime ($G < G_c$). The kinetics of subcritical interfacial delamination has been understood as controlled by stress-dependent chemical reaction in stage I and by mass transport of

environmental species (e.g., water molecules) to the crack tip in stage II [36]. Recently, by combining the kinetics of subcritical cracking and water diffusion, Tsui et al [47] proposed a model to predict degradation of adhesion in thin-film stacks as a function of exposure time to water and found good agreement with experimental data for film stacks containing a low-k dielectric material used in advanced integrated circuits.

4. Modeling of Chip-Packaging Interactions

Finite element analysis (FEA) is commonly used to evaluate the thermo-mechanical deformation and stress distributions in electronic packages and their impact on reliability. For stand-alone silicon chips, the modeling results show that thermal stresses in the Cu lines depends on its aspect ratio, i.e .the width vs height ratio, and the degree of confinement from the dielectric materials as well as the barrier and cap layers. For an aspect ratio greater than 1, the stress state is triaxial and behaves almost linear elastically under thermal cycling [73]. Wafer processing can induce additional residual stresses in the interconnect structures which has also been investigated using FEA [74]. The general behavior is in quantitative agreement with results from x-ray diffraction measurements [73, 75]. After the silicon die is assembled into a flip-chip package, the package deformation can increase the thermo-mechanical stresses in the interconnect structures. Modeling the packaging effect on the thermal stress of the interconnect structure is challenging due to the large difference in the dimensions of the

packaging and interconnect structures. For this reason, researchers from Motorola first introduced a multilevel sub-modeling technique to evaluate the energy release rate for interfaces in the interconnect structure after assembling the die into a flip-chip package [14, 15]. This technique bridges the gap between the packaging and wafer levels. The energy release rates for various interconnect interfaces during packaging assembly were calculated using 2D FEA models. However, a flip-chip package is a complicated 3D structure that cannot be properly represented using a 2D model. We developed, therefore, a 3D FEA model based on a 4-level sub-modeling technique to investigate the packaging effect on interconnect reliability, particularly focusing on the effects of low k dielectrics and other materials used to form the Cu interconnect structures [16, 19].

4.1. Multilevel Sub-Modeling Technique

Level 1: Starting from the package level, the thermal deformation for the flip-chip package is first investigated. At this package level, a quarter section of the package is modeled using the symmetry condition as illustrated in Figure 4.1a. No interconnect structure detail was considered at this level because its thickness is too small compared to the whole package. Simulation results for this package level model are verified with experimental results obtained from moiré interferometry.

Level 2: From the simulation results for the package level modeling, the most critical

solder bump is identified. A sub-model focusing on the critical solder bump region with much finer meshes is developed as shown in Figure 4.1b. The built-in cut boundary technique in ANSYS [76] is used for sub-modeling. At this sub-model level, a uniform ILD layer at the die surface is considered but still no detailed interconnect structure is included.

Level 3: Based on the Level 2 sub-modeling results, a large peeling stress is found at the die-solder interface. At the critical die-solder interface region with the highest peeling stress, a sub-model based on a Level 2 model is created using the cut boundary technique, as shown in Figure 4.1c. This sub-model focuses on the die-solder interface region (a small region of Level 2) containing a portion of the die, the ILD layer and a portion of the solder bump. Still only a uniform ILD layer at the die surface is considered at this level and no detailed interconnect structure is included.

Level 4: This sub-model zooms in further from the Level 3 model focusing on the die-solder interface region as shown in Figure 4.1d. Here a detailed 3D interconnect structure is included. An interconnect with two metal levels is considered first, and effects of multilevel stacks is discussed in Section 6. Ten lines are found to be sufficient to approximate the interconnect structure. The sub-model is set up accordingly and at the center line a crack with a fixed length is introduced along several interfaces of interest. Energy release rate and mode mix for each crack are determined using a modified virtual crack closure technique as discussed in the next section.

4.2 Modified virtual crack closure (MVCC) method

To investigate the impact of CPI on the reliability of low k interconnect and packaging structures, interfacial cracks are introduced in the models and the energy release rates as well as mode mix are calculated as a measure of the crack driving force for interfacial delamination. Several methods have been developed for calculating the interfacial fracture parameters within the framework of finite element analysis. The J-integral method has been widely used [77-79] and is a standard option in some commercially available FEA codes (e.g., ABAQUS [80]). This method is capable of calculating both the energy release rate and the mode mix for 2D and 3D interfacial cracks, but it requires relatively fine meshes near the crack tip to achieve convergence and path independence of the numerical results. A set of special finite element methods have also been developed to improve the numerical accuracy without requiring fine meshes, such as the singular element method [81], the extended finite element method (XFEM) [82], and an enriched finite element method [83, 84]. Implementation of these methods however is much involved numerically, which has been limited to problems with relatively simple geometry and material combinations. Alternatively, Liu et al. [23, 46] calculated stress intensity factors by comparing the crack surface displacement to the analytical crack-tip solution, from which both the energy release rate and mode mix were determined. This approach requires very fine meshes near the crack tip for

the accuracy of the displacement calculation, and is not readily applicable for 3D problems.

With the material and geometrical complexities in the four-level modeling of CPI, a simple method using standard FEA codes along with relatively coarse meshes is desirable for the fracture analysis. A modified virtual crack closure (MVCC) technique [85, 16] has emerged to meet such a need, and is described as follows.

As illustrated in Figure 4.2, the MVCC method calculates the components of the energy release rate corresponding to the three basic fracture modes 1, 2 and 3 separately. With the local stress/strain and displacement distributions obtained by the finite element modeling, both the energy release rate and the mode mix for the interfacial cracks can be calculated accordingly. For the eight-node solid elements shown in Figure 4.2, the three energy release rate components G_I , G_{II} and G_{III} can be obtained as:

$$\begin{aligned} G_I &= \sum_i F_z^{(i_1)} \delta_z^{(i_2)} / (2\Delta A) \\ G_{II} &= \sum_i F_x^{(i_1)} \delta_x^{(i_2)} / (2\Delta A) \\ G_{III} &= \sum_i F_y^{(i_1)} \delta_y^{(i_2)} / (2\Delta A) \end{aligned} \quad (4.1)$$

where $F_x^{(i_1)}$, $F_y^{(i_1)}$ and $F_z^{(i_1)}$ are nodal forces at node i_1 along the x, y and z directions, respectively, and $\delta_x^{(i_2)}$, $\delta_y^{(i_2)}$ and $\delta_z^{(i_2)}$ are relative displacements between node i_2 and node i_3 in the x, y and z directions, respectively. Note that for simplicity only one element set is shown along the crack front direction (y direction). The total energy release rate is then

$$G = G_I + G_{II} + G_{III}, \quad (4.2)$$

and the phase angles of mode mix may be expressed as

$$\begin{aligned}\psi &= \tan^{-1} \left[\left(\frac{G_{II}}{G_I} \right)^{\frac{1}{2}} \right] \\ \varphi &= \tan^{-1} \left[\left(\frac{G_{III}}{G_I} \right)^{\frac{1}{2}} \right]\end{aligned}\quad (4.3)$$

The criterion for interfacial delamination can thus be established by comparing the total energy release rate to the experimentally measured mode-dependent interface toughness, i.e., $G = \Gamma(\psi, \varphi)$.

While the original virtual crack closure technique (VCCT) was proposed for cracks in homogeneous materials [86-88], it has been shown that care must be exercised in applying the technique for interfacial cracks [88-92]. As noted by Krueger [88], due to the oscillatory singularity at the interfacial crack tip, the calculated energy release rate and mode mix may depend on the element size at the crack tip. It was suggested that the element size shall be chosen small enough to assure a converged solution by the finite element model but also large enough to avoid oscillating results for the energy release rate. Furthermore, as discussed in Section 3.2, the mode 1 and mode 2 in general cannot be separated for interfacial cracks (except for cases with $\beta = 0$). The separation of the energy release rate components in Eq. (4.1) is therefore dependent on the element size, and so is the definition of the phase angles in Eq. (4.3). The total energy release rate on the other hand was found to be less sensitive to the element size [89, 90]. Several approaches have been suggested to extract consistent phase angles of mode mix independent of the element size using the VCCT [91, 92], following the

standard definition in Eq. (3.6). For simplicity, the phase angles defined in Eq. (4.3) are used in the subsequent discussions.

4.3 Package level deformation

The FEA results for the package level modeling can be verified using results from moiré interferometry. Since the thermal load used in the moiré measurement was from 102°C to 22°C, we applied the same thermal load (102°C to 22°C) in the package level modeling in order to compare the moiré and FEA results. Figure 4.3 shows the z-displacement (package warpage) distribution along the die center line (Line A-A in Figure 2.1). The FEA and moiré results are found to be in good agreement. Detailed moiré results can be found in Reference 93.

4.4 Energy release rate for stand-alone chips

After verified with moiré interferometry, FEA was applied to evaluate the energy release rates for stand-along wafer structures as well as the packaging effect. Both Al and Cu interconnect structure with TEOS and a spin-on-polymer SiLK as ILD were investigated. The material properties used in the modeling analysis are listed in Table 1. All materials in the wafer structure were assumed to be linear elastic except at the package level where plasticity was considered for solder materials. To calculate the energy release rate, a crack was

introduced at several relevant interfaces as shown in Figure 4.4. The crack has a rectangular shape with a fixed length of $1.5 \mu\text{m}$ along the metal line direction and a width of $0.5 \mu\text{m}$, the same as the metal line width and thickness. In general, the energy release rate depends on the number of the metal levels and the crack dimension used in the calculation. In the following discussion, a fixed crack size in a two-level structure is used in order to simplify the CPI computation in the study of the material and processing effects. This point should be kept in mind as the crack driving force is compared, particularly when the CPI study is extended to four-level interconnect structures with a different crack size to study scaling and ULK effects in Section 6.

Table 4.1 Mechanical properties of interconnect materials

Material	E (GPa)	ν	α (ppm/ $^{\circ}$ C)
Si	162.7	0.28	2.6
Al	72	0.36	24.0
Cu	122	0.35	17.0
TEOS	66	0.18	0.57
SiLK	2.45	0.35	66.0
MSQ	7.00	0.35	18.0
CVD-OSG	17	0.35	8
Porous MSQ-A	2	0.35	10
Porous MSQ-B	5	0.35	10
Porous MSQ-C	10	0.35	12
Porous MSQ-D	15	0.35	18

The energy release rates for interfacial fracture along the six interfaces shown in Figure 4.4 were first calculated for the stand-alone chip subjected to a thermal load of 400 $^{\circ}$ C to 25 $^{\circ}$ C, typical for wafer processing. The results summarized in Figure 4.5 show that the energy release rates for all the interfaces in Al/TEOS and Cu/TEOS structures are generally small, less than 1 J/m². The Cu/SiLK structure has the highest energy release rates for the two

vertical cracks along the SiLK/barrier sidewall (Crack 2) and along the barrier/Cu interfaces (Crack 3), both exceeding 1 J/m^2 . The fracture mode for these two cracks is almost pure mode I, indicating that for the stand-alone chip, the tensile stresses driving crack formation act primarily on the vertical interfaces due to the large CTEs of the low k ILDs in comparison to the CTEs of the silicon substrate and metal lines. Comparing to the critical energy release rates for low k interfaces obtained from experiments (usually about $4\text{-}5 \text{ J/m}^2$ [12]), these values are considerably lower. Hence, interfacial delamination in Cu/low k interconnect structures during wafer processing is not expected to be a serious problem although the result does not rule out the possibility of delamination due to subcritical crack growth.

5. Energy Release Rate under Chip-Package Interactions

5.1 Effect of Low k Dielectrics

The energy release rates induced by CPI were evaluated using the 4-step multilevel sub-model. A stress-free state was assumed at -55°C for the flip-chip package and the crack driving force was obtained at 125°C to simulate a test condition of -55°C to 125°C . The package used has the same dimensions as the one used for moiré measurements, which has a plastic substrate with a die size of $8\text{x}7 \text{ mm}^2$ and lead free solders (95.5Sn/3.8Ag/0.7Cu). The critical solder bump with the highest thermal stress is the outermost one close at the die

corner. The interconnect structure located at this critical solder bump/die interface was investigated. The results are given in Figure 5.1, which reveal a small CPI effect for Al/TEOS and Cu/TEOS structures. In contrast, the effect is large for the Cu/SiLK structure with the crack driving force G reaching 16 J/m^2 . Interestingly, the interfaces parallel to the die surface (Crack 1, 4, 5 and 6) are more prone to delamination instead of the vertical interfaces 2 and 3 as for the stand-alone chip. For these parallel interfaces, the mode mix is close to being a pure mode I although for the Cu/passivation interface, both mode I and III components are present. Comparing with the results for the stand-alone wafers and that after packaging, not only a large increase in the crack driving force is evident due to chip-package interactions, the interfaces most prone to delamination also change to those parallel to the die surface. This indicates that the crack driving force becomes dominated by thermal stresses imposed by the package deformation where the package warpage has the most significant effect for the parallel interfaces.

For the Cu/SiLK interconnect structure, packaging seems to have a significant impact on interconnect reliabilities as shown in Figure 5.1. The crack driving force can be as high as 16 J/m^2 after packaging assembly, therefore interfacial delamination can become a serious problem for the Cu/SiLK structure. From Figure 5.1 we see that the crack driving force along interfaces parallel to the die surface (Crack 1, 4, 5 and 6) is significantly enhanced by chip-

package interaction. For interfaces 1, 5 and 6, the crack driving force induced by CPI is very close to being pure mode 1 although a mix mode is found for the Cu/PASS interface (Crack 4). These results indicate that the delamination induced by CPI occurs near the outermost solder balls under mostly a mode 1 condition. As the crack propagates, both the energy release rate and the mode mix at the crack tip vary. It will follow a path that maximizes G/Γ , the ratio between the energy release rate and the fracture toughness. Depending on the local material combination and wiring geometry, the crack will zigzag through the interconnect structure toward the lower Cu levels with weaker low k dielectrics. As the crack propagates, the energy release rate will increase while the phase angle changes to mix mode depending on the local wiring geometry. The crack propagation problem in an interconnect structure is complex and will be further discussed in Section 6.

5.2 Effect of solder materials and die attach process

As the semiconductor industry shifts from Pb-based solders to Pb-free solders, the effects of solder materials on CPI and low k interconnect reliability become of interest. The energy release rates for the six interfaces are compared in Figure 5.2 for high lead (95Pb/5Sn), eutectic lead alloy (62Sn/36Pb/2Ag) and lead-free solder (95.5Sn/3.8Ag/0.7Cu). The material properties used in these calculations are shown in Table 2. The mismatch in CTE between the lead-free solder and underfill is larger than that between the high lead or eutectic solder and

underfill. The Young's modulus of the lead-free solder is also larger than the high lead and eutectic solders. Thus larger thermal stresses are induced at the die surface for the lead-free solder package comparing to the high lead and lead eutectic solder packages, resulting in the highest driving force for interconnect delamination in lead-free packages.

Table 5.1 Material Properties for high-lead, eutectic lead and lead-free solders

Solder Material	E (GPa)	ν	α (ppm/ $^{\circ}$ C)
Eutectic	$75.84 - 0.152 * T$	0.35	24.5
High lead	$39.22 - 0.063 * T$	0.35	29.7
Lead-free	$88.53 - 0.142 * T$	0.40	16.5
Underfill	6.23	0.40	40.6
Organic substrate	Anisotropic elastic		16(in plane) 84(out of plane)

The processing step with the highest thermal load in flip-chip package assembly is the die attach before underfilling the package. The solder reflow occurs at a temperature higher than the solder melting point and afterwards the package structure is cooled down to room temperature. Without the underfill serving as a stress buffer, the thermal mismatch between the die and the substrate can generate a large thermal stress at the solder/die interface

near the die corner driving interfacial delamination. The CPI effect of the die attach step for low-k structure was investigated for Cu/SiLK and Cu/MSQ structures for different solder materials. Here the study was again performed for the high lead, eutectic lead and lead-free solders with different reflow cycles: 160°C to 25°C for eutectic solder, 250°C to 25°C for lead-free solder and 300°C to 25°C for high lead solder. The substrate in the package was organic and with a die size of 8x7 mm² and the study assumed that the high lead solder can be assembled onto an organic substrate in order to compare these solders on the same substrate. Results are summarized in Figure 5.3a for Cu/SiLK chips assembled on an organic substrate. The eutectic solder package has the lowest crack driving force for interfacial delamination due to its lowest reflow temperature. In contrast, the lead free solder package is most critical due to the high reflow temperature and the high Young's modulus of the lead free solder material. For the high lead solder, although it has the highest reflow temperature, but with the lowest Young's modulus, the crack driving force is lower than that for the lead free solder package. For comparison, the results for the Cu/MSQ structure with eutectic and lead-free solders are shown in Figure 5.3b. The energy release rate for the Cu/MSQ structure is generally about a factor of 3 lower than that of the Cu/SiLK structure. This can be attributed to the 3x higher Young's modulus of the MSQ dielectrics, indicating that the mechanical property of the low k is an important factor to consider for the packaging effect.

Comparing Figure 5.2 and Figure 5.3a, it is clear that the crack driving force in the

Cu/SiLK structure during the die attach process is generally larger than that in an underfilled package during thermal cycling from -55°C to 125°C. This indicates that the die attach process with a larger thermal load is a more critical step than thermal cycling in driving critical interfacial delamination in Cu/low k structures.

5.3 Effect of low k material properties

To investigate the effect of dielectric properties, we first compare the CPI for a CVD-OSG ($k = 3.0$) [8] with an MSQ [9] and a spin-on polymer SiLK [6] to investigate how better material properties can improve interconnect reliability. Both MSQ and SiLK are fully dense with $k \sim 2.7$. The energy release rates were computed using the two-level interconnect structure with Cracks 1 to 6 and the results are plotted in Figure 5.4. Among the dielectric materials, the ERR driving forces are the lowest for CVD-OSG, which has the highest Young's modulus (E). For the spin-on polymer which has the lowest E, the ERR values for Cracks 1 and 6 are about 6 times higher than that of CVD-OSG. This indicates that the on-chip interconnect fabricated with spin-on polymer needs about 6 times higher adhesion strength at the interfaces of Cracks 1 and 6 in order to obtain a mechanical reliability equivalent to interconnects fabricated using CVD-OSG.

Next the study is extended to several porous MSQ materials (A to D) [10] which are being developed for interconnect structures of the 65 nm node and beyond. These porous low

k materials have k less than 2.3 but with different thermomechanical properties which are listed in Table 1. The results are plotted in Figure 5.5, which shows a good correlation between ERR and E . Comparing porous MSQ-D ($k = 2.3$) with fully dense CVD-OSG ($k = 2.7$), both with similar mechanical properties, their ERR values are similar. Interestingly, for the porous MSQ-A and the spin-on-polymer, even though they have very different CTE but with similar E , their ERR values are about the same too. Overall, there seems to be little effect due to the CTE of the low k materials. In contrast, the ERR increases considerably with decreasing E . Therefore, for low k dielectrics, increasing E seems to be effective for improving the mechanical reliability.

The interconnect structure used to calculate ERR in this study is a simple two-layer structure. The actual interconnect structure for low k chips for the 65nm technology node will have more than 11 layers and with complex geometry and material combinations [12]. There will be other interesting and important factors contributing to ERR to affect package reliability. Of particular interest is channel cracking induced by thermal stress in compliant low k layers, which depends on the interconnect geometry and layer stack structure. There will also be the effect due to residual stresses generated by thermal processing during chip fabrication, which can superimpose onto the CPI stresses to affect the ERR driving force. [48, 74]

6. Effect of Interconnect Scaling and Ultra Low k Integration

The scaling of interconnect structures has led to highly complex architectures with over 10 metal layers, sub-50 nm dimensions, and ultra low k dielectrics (ultimately airgap structures). There are important questions regarding the effect of interconnect scaling and the implementation of ultra low k dielectric on chip-package interaction and low k interconnect reliability. The study of the scaling effect is focused on two issues: the first is on the effect of implementation of ultra low k dielectric and the second is to study the effect of interconnect geometry on the ERR as the crack propagates through the Cu low k structure. Previous studies have investigated the effect of increasing stacking layers based on 2D multilevel sub-models and found that the ERR increases with addition of more wiring levels [15, 20]. The study reported here is based on a 3D multilevel interconnect model with four metal levels, as shown in Figure 6.1. We found that a 4-level 3D structure provides a realistic wiring structure to analyze the effect of porous low k implementation in the interconnect structure. In this structure, the pitch and line dimensions in the first two metal layers (M1 and M2) are doubled in the third layer (M3), which are doubled again in the fourth layer (M4), simulating the hierarchical layers in real interconnect structures.

The effect of ultra low k implementation was investigated using different stacking of low k and ultra low k dielectric layers. In this study, we are interested to find out whether different combinations of low k and ultra low k dielectrics in selective metal layers could

improve mechanical reliability without sacrificing electrical performance (RC delay). Energy release rates were calculated for horizontal cracks placed at each metal level at the interface between the etch stop/passivation (ESL) and the low k dielectric, which is known to be most prone to delamination. Each crack has a width of 0.1 μm and a length of 2 μm extending in the multiple wiring direction as shown in Figure 6.1. Results of the ERRs of the interfacial cracks in the four-level interconnect models with three different ILD combinations are summarized in Figure 6.2. The first model (Fig. 6.2a) uses ultra low k materials in all layers, for which the interfacial crack at the upmost level (crack 4) has the largest ERR. This is to be expected since the upmost level is the thickest, 4X of the M1 thickness, and thus the maximum crack driving force. In the second model (Fig. 6.2b), SiO_2 is used to replace ULK at level 4. In this case, the high E of SiO_2 significantly reduces the ERR of crack 4, but raises the ERRs in the other three interfaces. This reflects the effect on the crack driving force due to the elastic mismatch between SiO_2 and the ULK layer as discussed in Section 3.2. In this structure, the ERR is highest for Crack 3 in the M3 level which is thicker than M1 and M2. In model 3 (Fig. 6.2c), a fully dense low k CVD OSG is used at level 3, which has a higher E than the ULK. Consequently, the ERR of crack 3 is reduced and the effect of elastic mismatch shifts the largest ERR to Crack 2 in the M2 level with a magnitude comparable to that of crack 3 in Model 2. This set of results indicates that the ultra low k interface at the upmost level is the most critical and the multilevel stacking structure has to be optimized in

order to minimize the CPI effect on ULK interconnect reliability.

As shown in Fig. 6.3, the calculated energy release rates increases dramatically from low k (OSG and NCS) to ultra low k ILDs, especially for cracks 2 and 3. This trend is consistent with the results from the two-level interconnect model, which has shown increasing ERRs with decreasing ILD modulus (Fig. 4.4). However, the magnitudes of the ERRs in the four-level model are considerably lower than those obtained from the two-level model, possibly due to denser metal lines providing stronger constraint on the cracks. Since ultralow k materials are required for 45nm technology and beyond, this result indicates that CPI will be a major concern due to the weak mechanical properties of the ultralow k materials.

As a crack propagates in a multilevel interconnect structure, both the energy release rate and the mode mix at the crack tip vary. As illustrated by a two-dimensional model in Figure 6.4, as the crack grows from right to left along one interface, the energy release rate oscillates as a function of the crack length. When the crack tip is located close to the left corner of a metal line, the energy release rate peaks. The magnitude of the peak increases with the crack length, but seems to saturate toward a steady state. The phase angle oscillates as well, but within a relatively small range. Apparently, the local material combinations and geometry complicate the stress field near the crack tip and thus the crack propagation along the interface. As a conservative design rule, the maximum energy release rate must be kept

below the interface toughness at the corresponding mode mix to avoid interfacial delamination.

A crack propagation in a real interconnect structure due to CPI is shown in Figure 6.5.

Apparently, the crack does not always propagate along one interface. Depending on the local material combination and geometry, an interfacial crack may kink out of the interface, causing cohesive fracture of low k materials. Similarly, a cohesive crack may deflect into a weak interface. The selection of the crack propagation path depends on the loading conditions as well as material properties (including interfaces) and geometrical features in the interconnect structure. A general rule of crack propagation, as suggested by Hutchinson and Suo [26] for anisotropic materials and composites, may be stated as follows: a crack propagates along a path that maximizes G/Γ , the ratio between the energy release rate and the fracture toughness. While cohesive fracture in an isotropic material typically follows a path of mode I ($\psi = 0$), the mode mix along an interfacial path varies and so does the interfacial fracture toughness. Therefore, the crack propagation not only seeks a path with the largest energy release rate, but also favors a path with the lowest fracture toughness, either interfacial or cohesive. Due to the complexity in the materials and structures, modeling of crack propagation in multilevel interconnects has not been well developed. Experiments have shown that cracks often propagate from upper levels to lower levels, eventually causing failure by die cracking. Figure 6.6 depicts a simple model of crack propagation in a

multilevel interconnect due to CPI. The crack initiates at an upper level interface, which has been shown to have a higher energy release rate compared to the same crack in a lower level interface. As the crack propagates toward the lower levels and the total crack length increases, the energy release rate increases. Without detailed data of the interface toughness, the calculation of the energy release rate alone is not sufficient to predict the crack propagation path. Nevertheless, it illustrates a possible scenario in consistency with experimental observations.

7. Summary

Chip-package interaction has become a critical reliability issue for Cu low k chips during assembly into plastic flip-chip packages, particularly for ultra-low k porous dielectrics to be implemented beyond the 65 nm node. In this paper, we review the experimental and modeling studies to investigate the chip-package interaction and its impact on low k interconnect reliability. The problem is explored using high-resolution moiré interferometry and multi-level sub-modeling and its origin is traced to the large thermal stress induced by package deformation to drive crack propagation and the weak thermomechanical properties of the low k dielectric material. The nature of interfacial delamination and crack growth in multilayered dielectric structures was discussed based on fracture mechanics. The chip-package interaction was investigated using 3D finite element analysis (FEA) based on a

multilevel sub-modeling approach. The packaging induced crack driving force for relevant interfaces in Cu/low k structures was deduced. The die attach process was found to be a critical step and the energy release rate was found to depend on the solder, underfill and low k material properties. Finally the effect of scaling and crack propagation in multiple Cu/dielectric line structures was investigated. Crack propagation was found to be a complex phenomenon depending on the local material combinations and geometry which controls the stress field near the crack tip and thus the crack propagation along the interface.

While the recent effort from industry and universities has significantly advanced the present understanding of chip-package interaction and its reliability impact on Cu low k interconnects. Many questions remain and a major challenge in microelectronics packaging is to prevent cracks initiated at the edge of a chip from propagating into the functional area of the chip under thermomechanical loadings during packaging processes and service. The use of low k and ultralow k dielectrics in the interconnects presents even more of a challenge due to chip-package interactions and significantly lower toughness of the low k materials. One approach to preventing propagation of the edge cracks is to incorporate patterned metal structures around the perimeter of a chip as the crackstop structure. If designed properly, the metal structures can increase the fracture toughness along the path of crack propagation. A four-point bend experiment has been used to determine the effective toughness of crackstop structures [42]. The optimal design of crackstop structures requires better understanding of

crack propagation under the influence of chip-package interactions.

Acknowledgments

The authors are grateful for the financial support for their research from the Semiconductor Research Corporation, the Fujitsu Laboratories of America and the United Microelectronics Corporation. Fruitful discussions with many colleagues including R. Rosenberg, M. W. Lane, T. M. Shaw and X. H. Liu from IBM, E. Zschech and C. Zhai from AMD, J. H. Zhao and D. Davis from TI, G. T. Wang and J. He from Intel, C. J. Uchibori and T. Nakamura from Fijitsu Laboratories, Z. Suo from Harvard, H. Nied from Lehigh and R. Dauskardt from Stanford are also gratefully acknowledged.

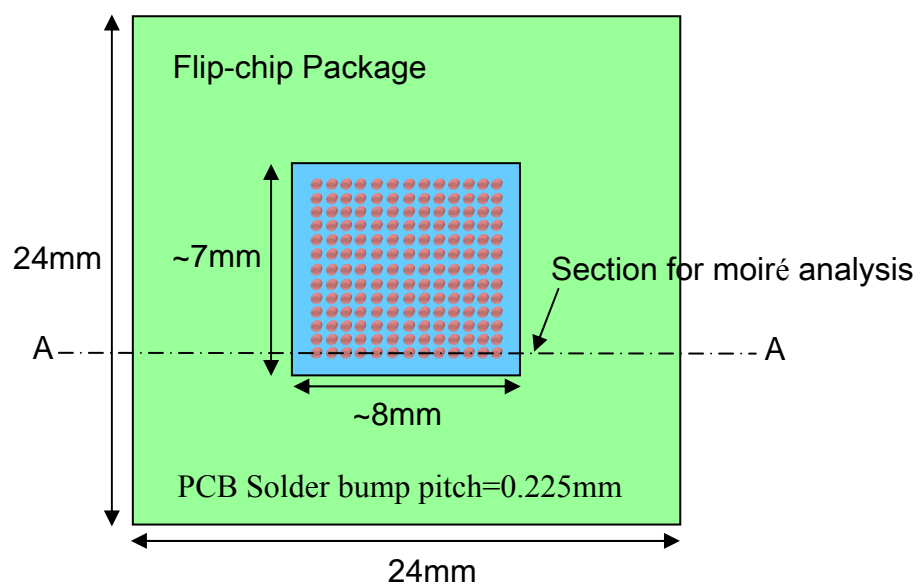
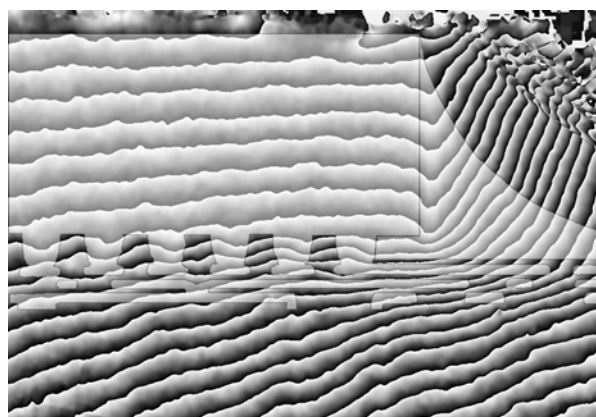


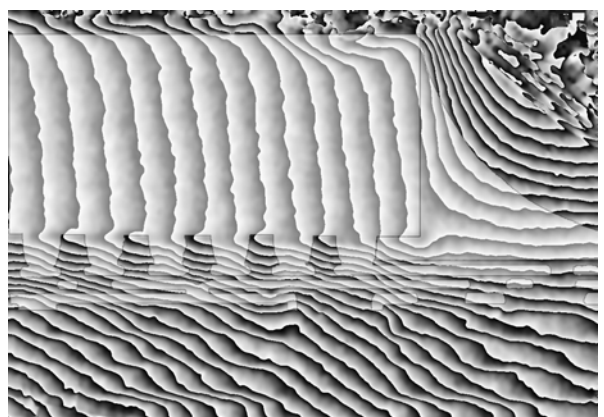
Fig. 2.1. Schematic of a flip-chip package for moiré interferometry study, where the optical grating was attached to the cross section as indicated for moiré measurements.



Fig. 2.2. Optical micrograph for the package cross-section used for moiré interferometry study.



(a)



(b)

Fig. 2.3. Phase contour maps obtained by high-resolution moiré interferometry for the flip-chip package in Fig. 2.1: (a) u field and (b) v field.

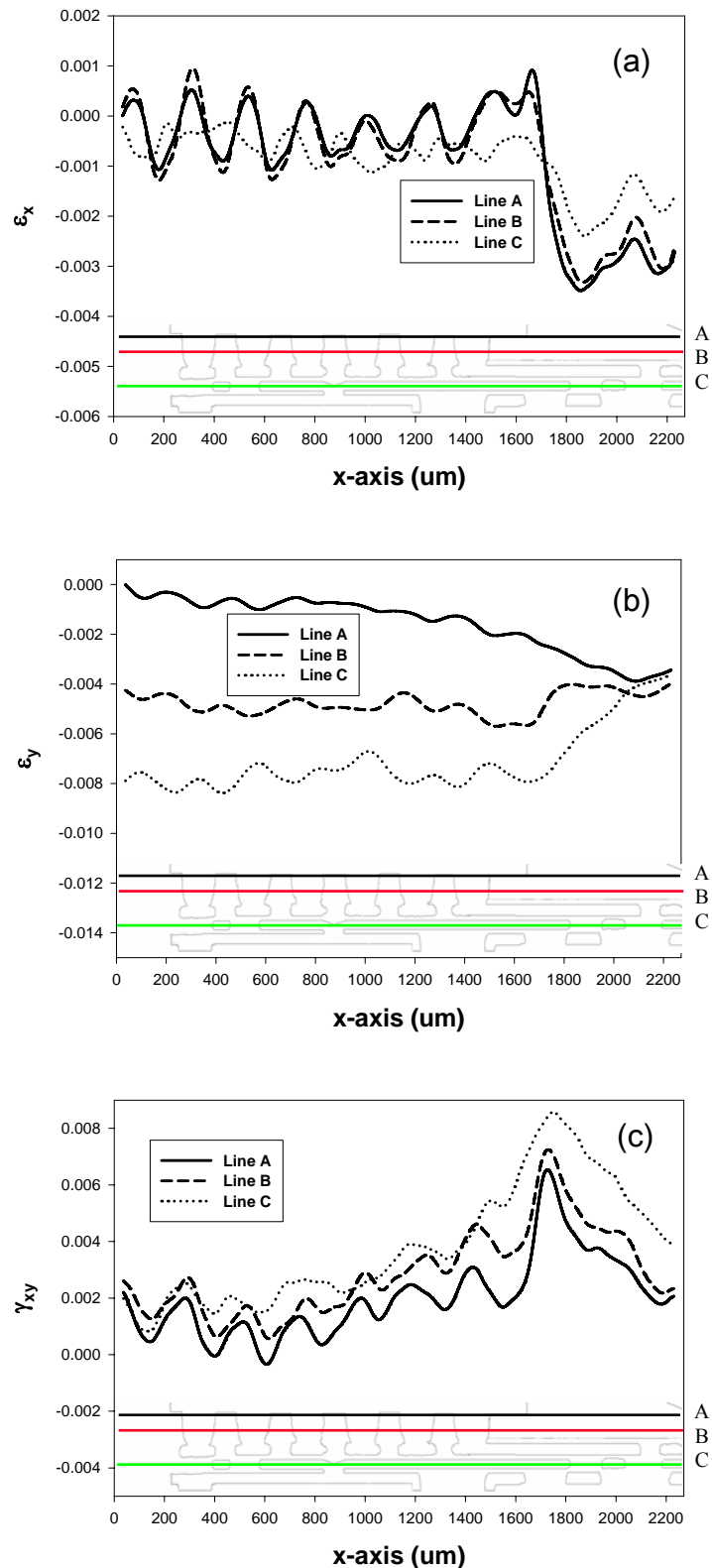


Fig. 2.4. Distributions of strains induced by chip-package interaction along three lines: the silicon-solder interface (Line A), the centerline of solder bumps (Line B) and the centerline of the high density interconnect wiring layer above the BT substrate (Line C).

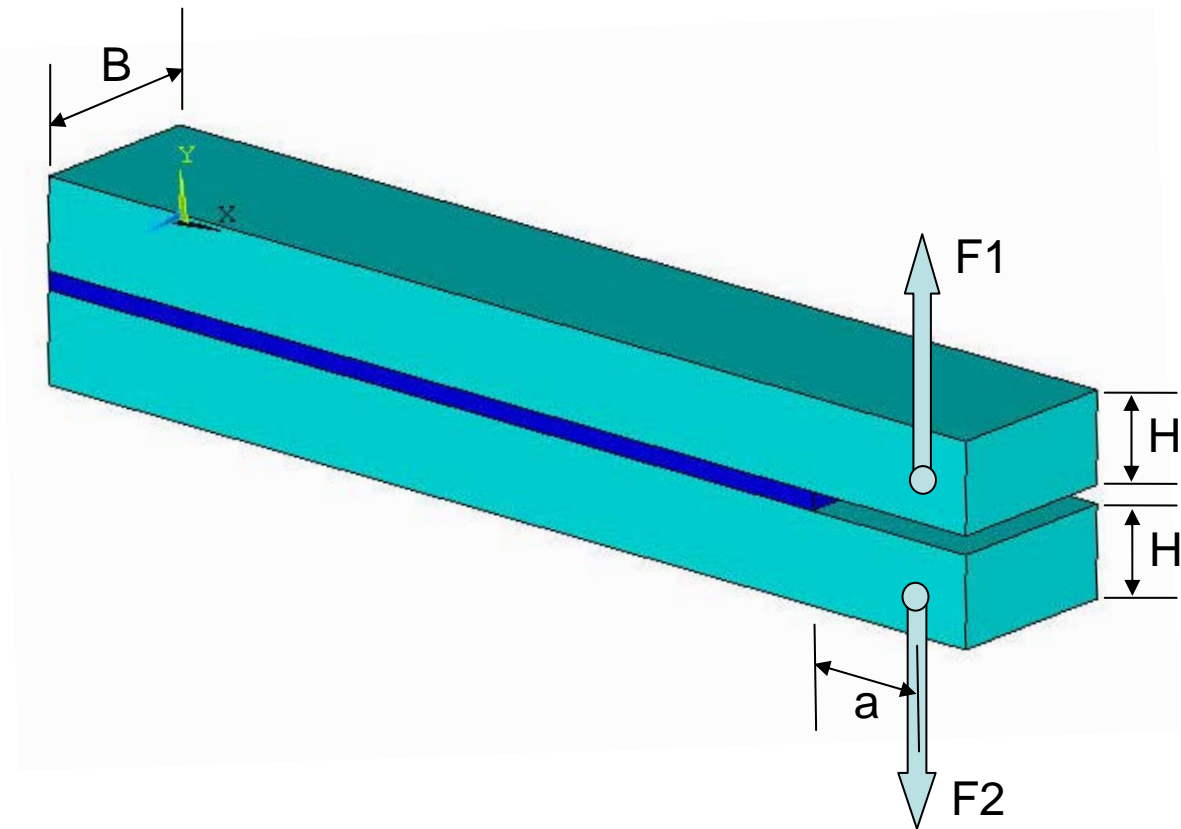


Fig. 2.5. Schematic of a double cantilever beam specimen. For symmetric DCB tests, $F_1 = F_2 = P$. For mixed-mode DCB tests, the two forces can be adjusted independently (see Fig. 2.7).

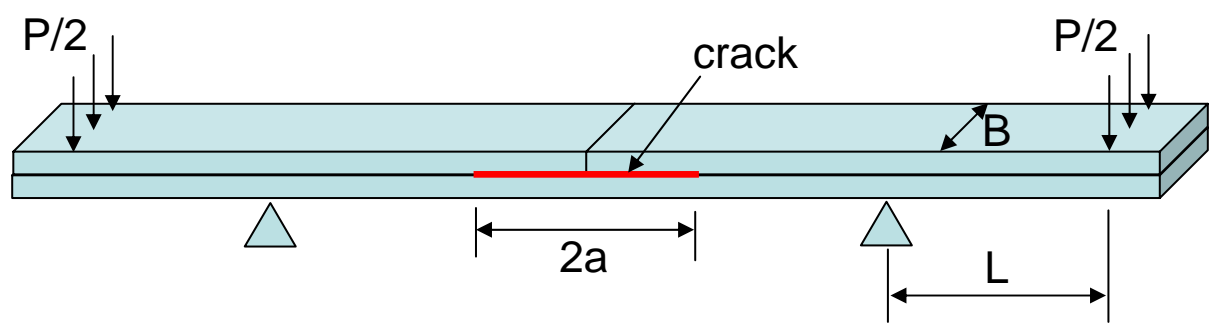


Fig. 2.6. Schematic of a four-point bending test.

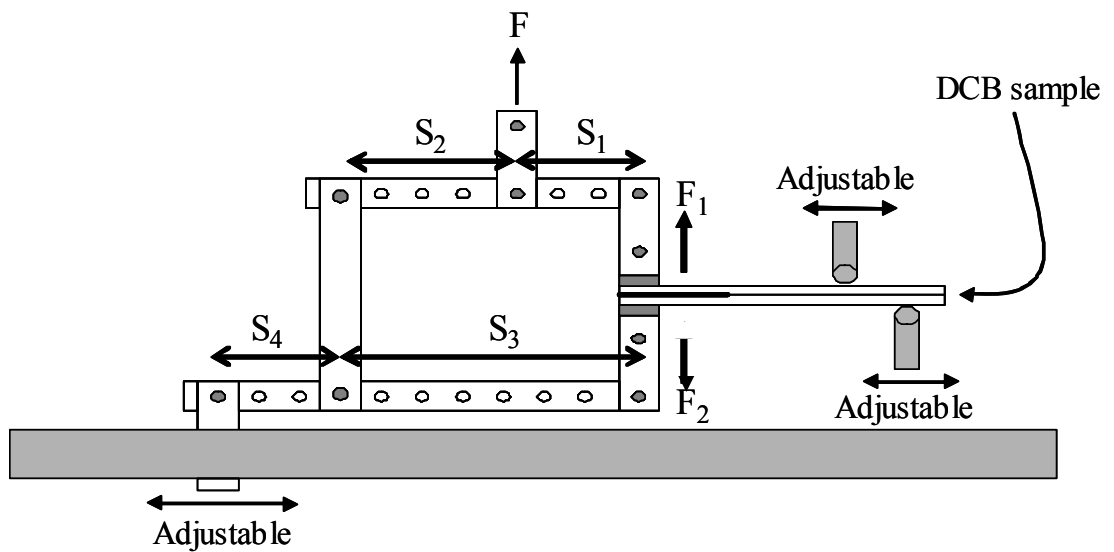


Fig.2.7. Mixed-mode double cantilever beam test loading fixture

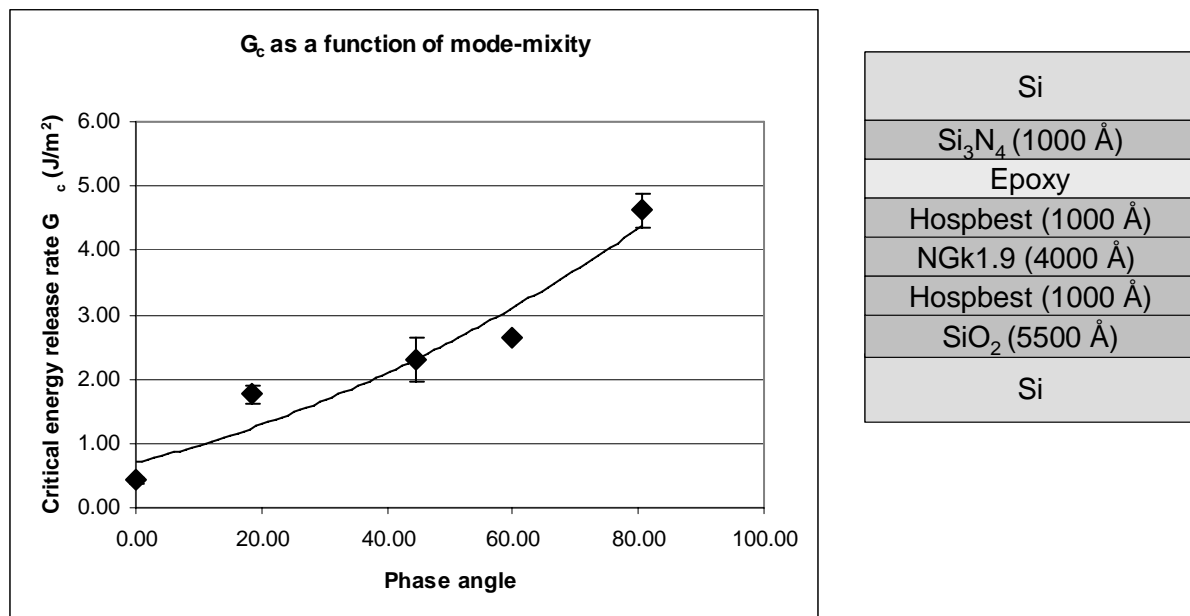


Fig. 2.8. Interface toughness as a function of the mode mix measured by the mixed-mode DCB tests. The inset shows the Si/SiO₂/Hospbest/low k(NGk1.9)/Hospbest film stack with the film thicknesses, where Hospbest is a siloxane-based hybrid material.

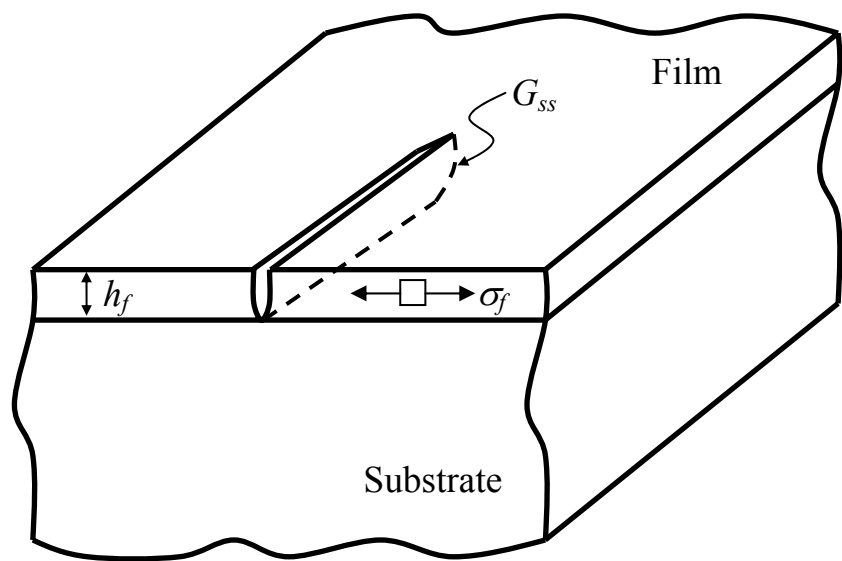


Fig. 3.1. Illustration of a channel crack.

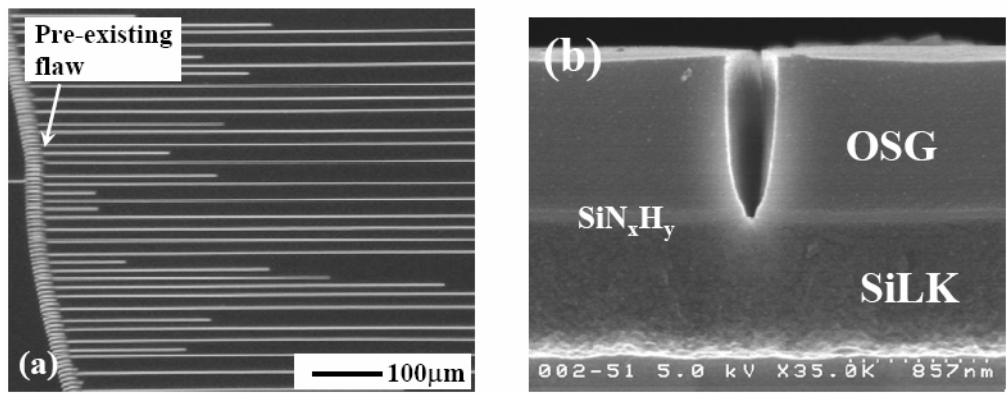


Fig. 3.2. Top view (a) and cross-sectional view (b) of channel cracks in thin film stacks of low k materials [48].

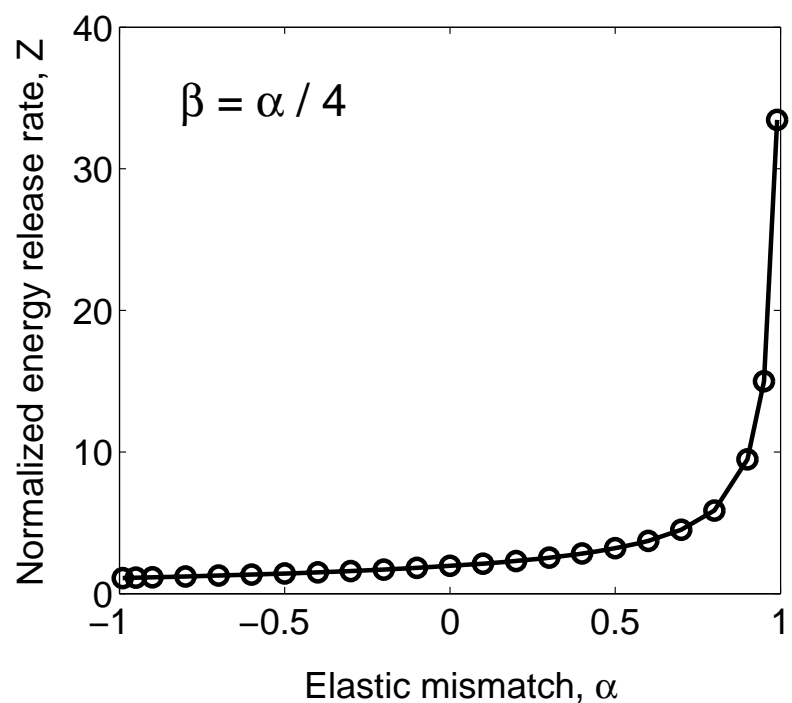


Fig. 3.3. Normalized energy release rate for steady state channel crack growth.

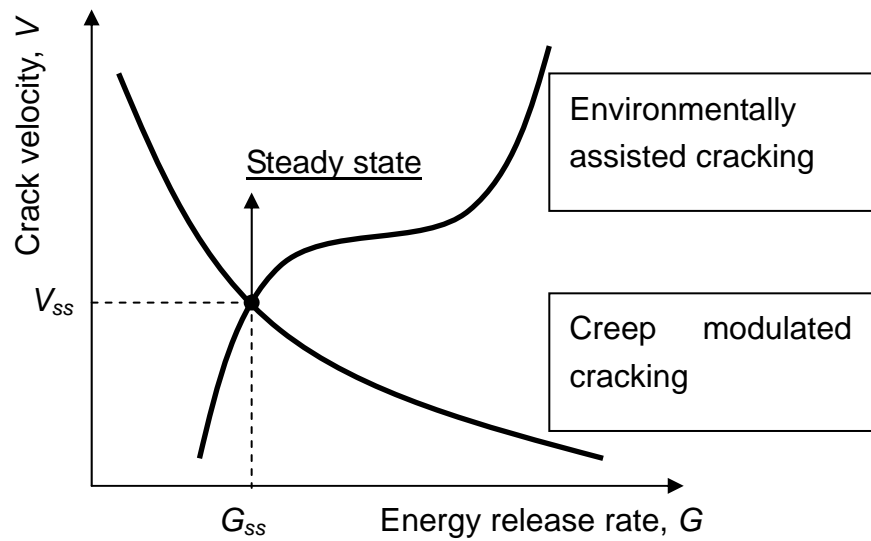


Fig. 3.4. Schematic illustration of the V-G relationships for environmentally assisted cracking and creep modulated cracking in thin films.

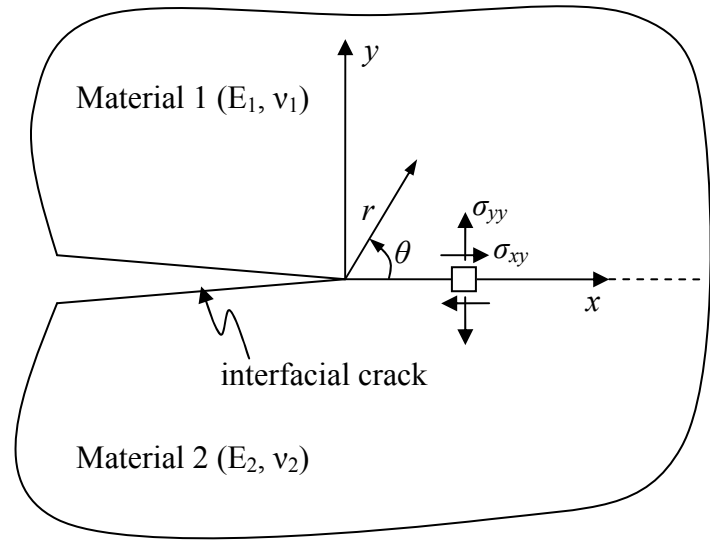


Fig. 3.5. Geometry and convention for an interfacial crack

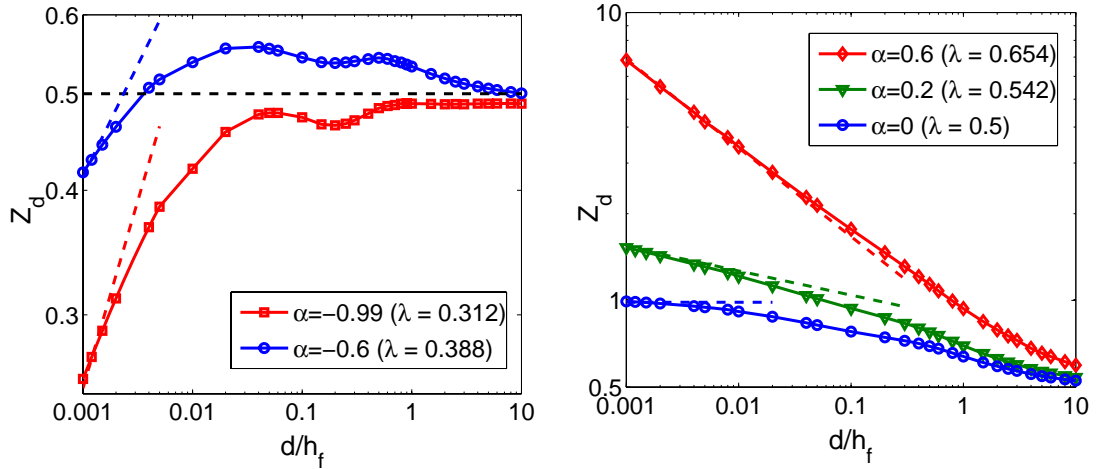


Fig. 3.6. Normalized energy release rate of interfacial delamination ($Z_d = G_d \bar{E}_f / (\sigma_f^2 h_f)$) from the root of a channel crack as a function of the interfacial crack length. (a) $\alpha < 0$, and (b) $\alpha \geq 0$. The dashed lines indicate the asymptotic solution given by Eq. (3.10), and $Z_d = 0.5$ for the steady-state delamination.

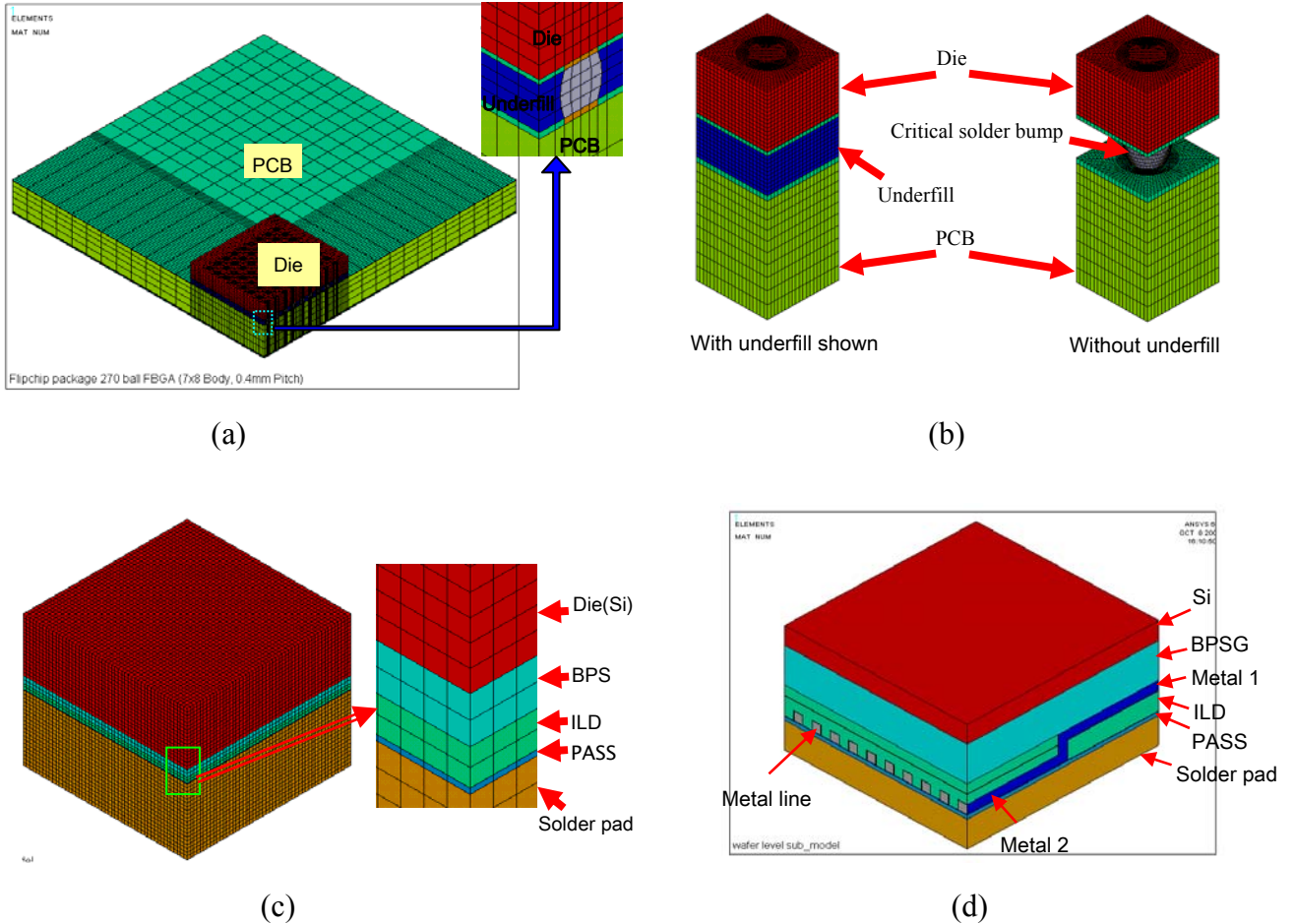


Fig. 4.1. Illustration of four-level sub-modeling: (a) package level; (b) critical solder level; (c) die-solder interface level; (d) detailed interconnect level.

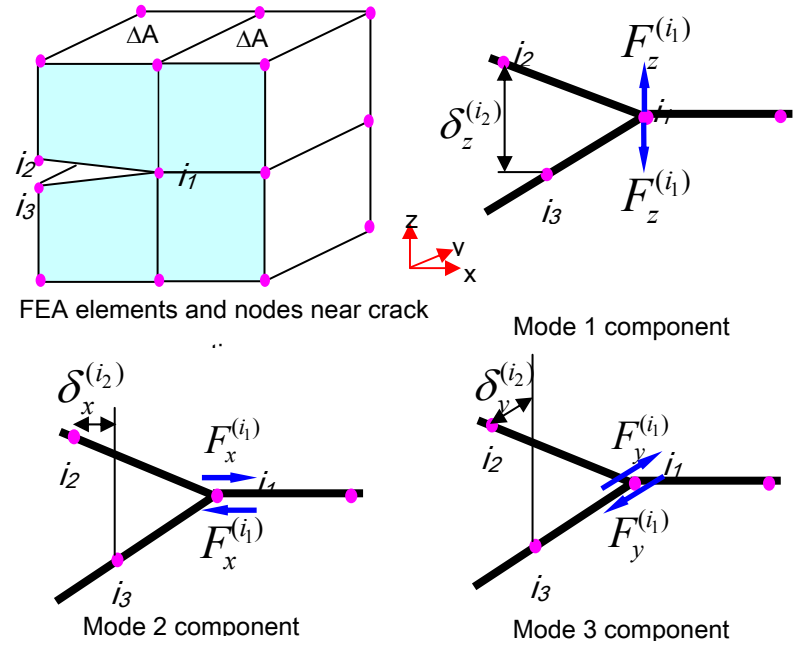


Fig. 4.2. Illustration of the modified virtual crack closure (MVCC) technique

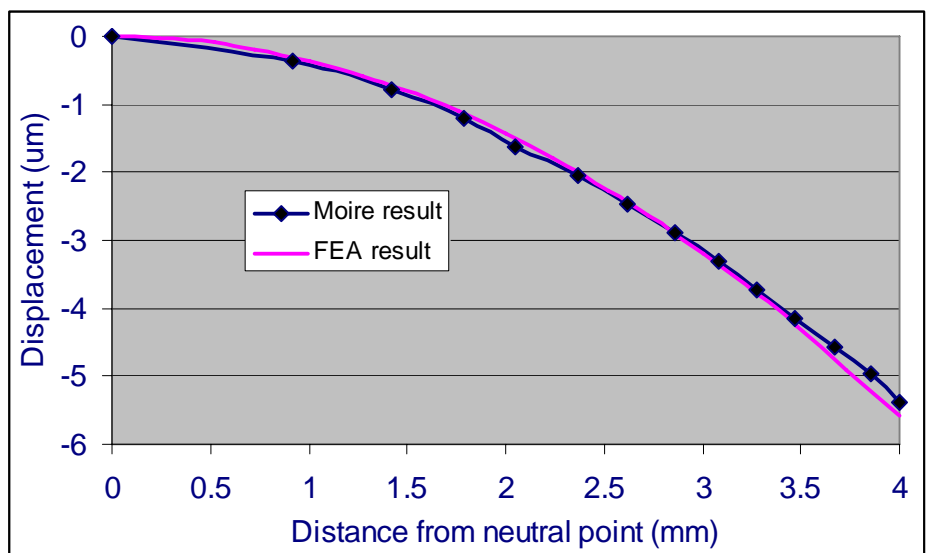


Fig. 4.3. Comparison of FEA and Moiré results of thermal deformation for the flip-chip package in Fig. 2.1.

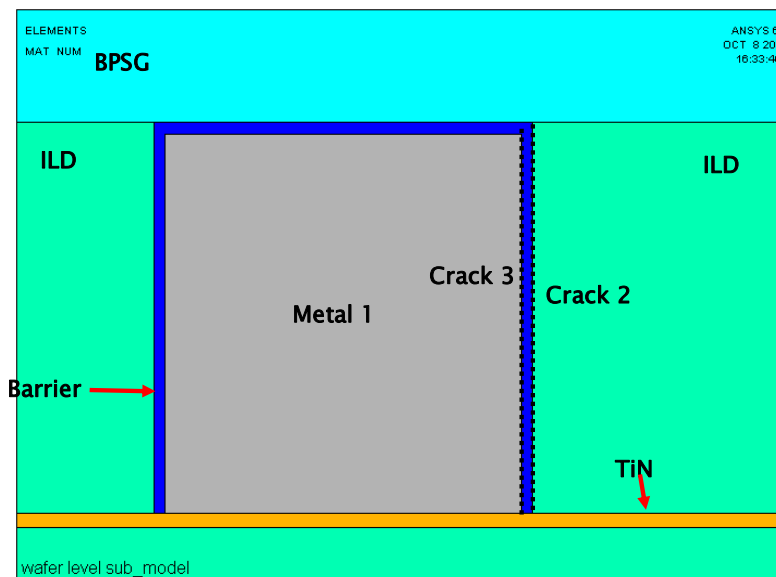
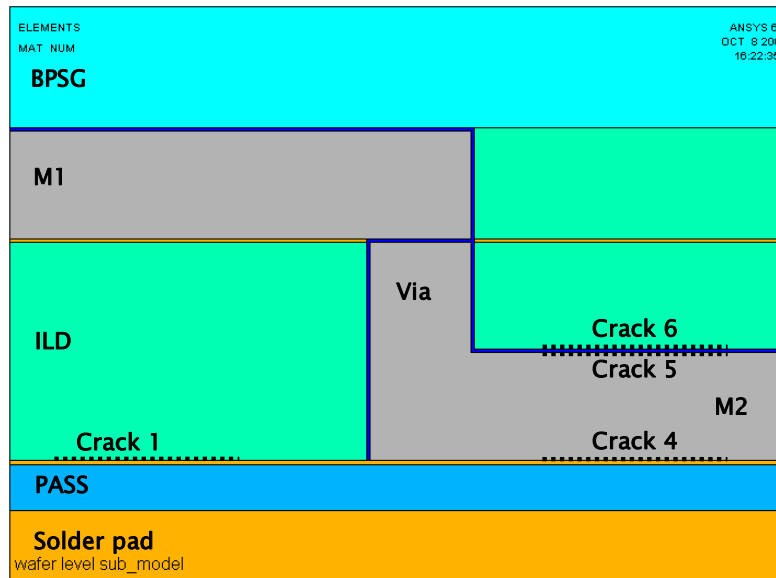


Fig. 4.4. Cracks introduced along interfaces of interest

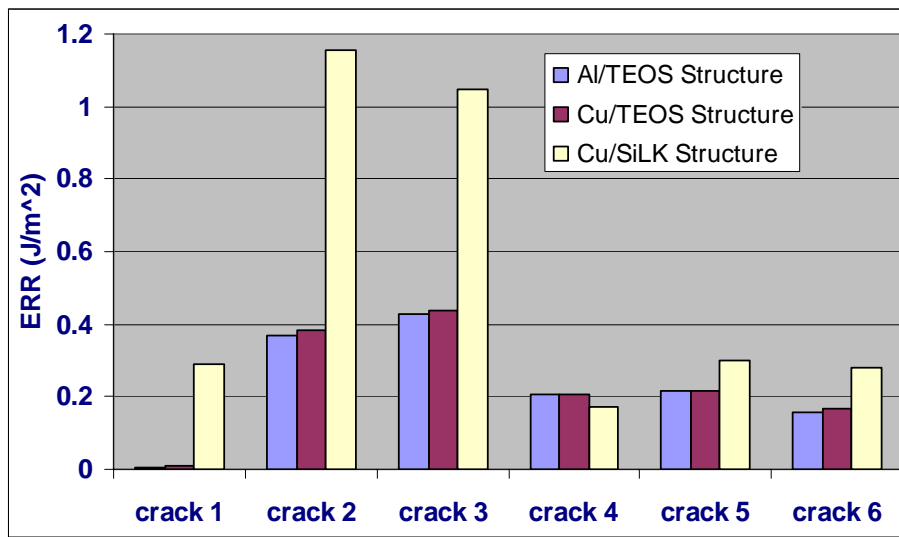


Fig. 4.5. Energy release rates for interfaces in interconnect structures in stand-alone chip before packaging assembly (from 400°C to 25°C)

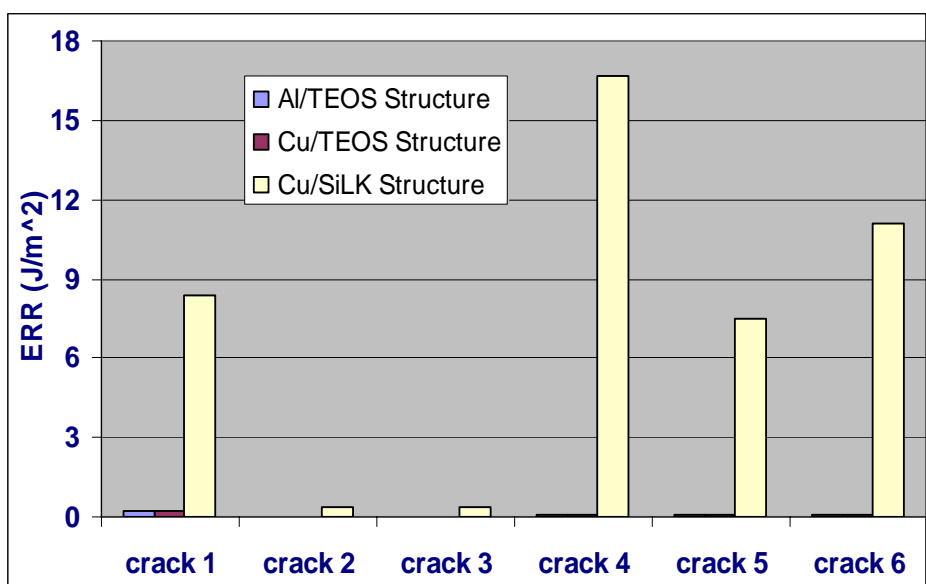


Fig. 5.1. Energy release rates for interfaces in on-chip interconnect structures after packaging assembly

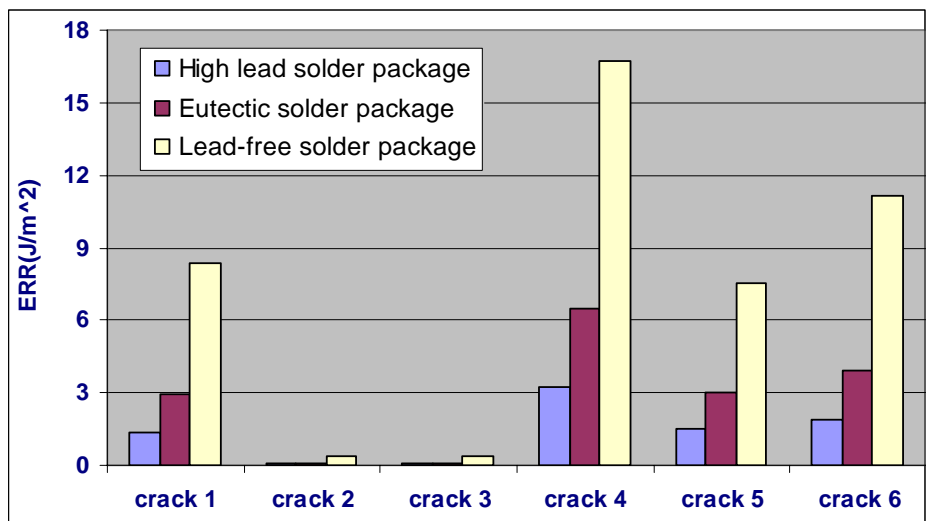
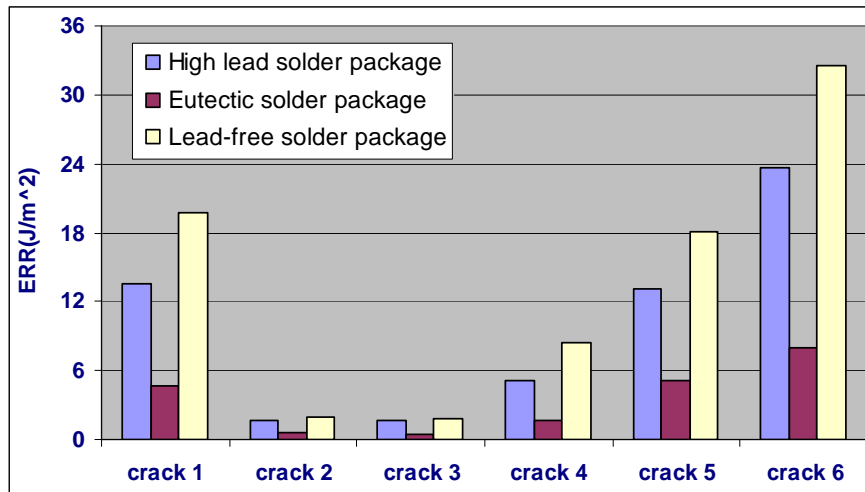
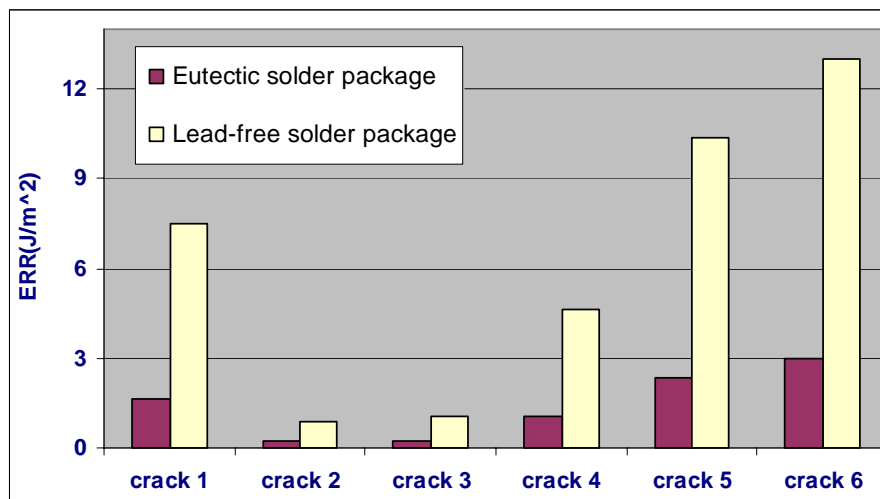


Fig. 5.2. Energy release rates for Cu/SiLK interconnect structures in high lead, eutectic solder and lead-free solder packages



(a)



(b)

Fig. 5.3. Energy release rates for interconnect interfaces in (a) Cu/SiLK and (b) Cu/MSQ structures in die attach process.

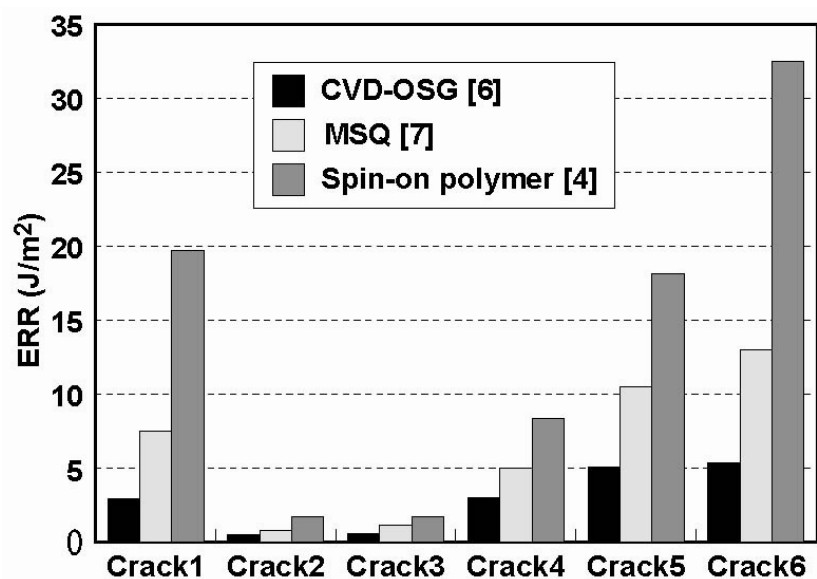


Fig. 5.4. Comparison of ERR for low k dielectrics of CVD-OSG, MSQ and a spin-on polymer. The cracks are the same as shown in Figure 4.4.

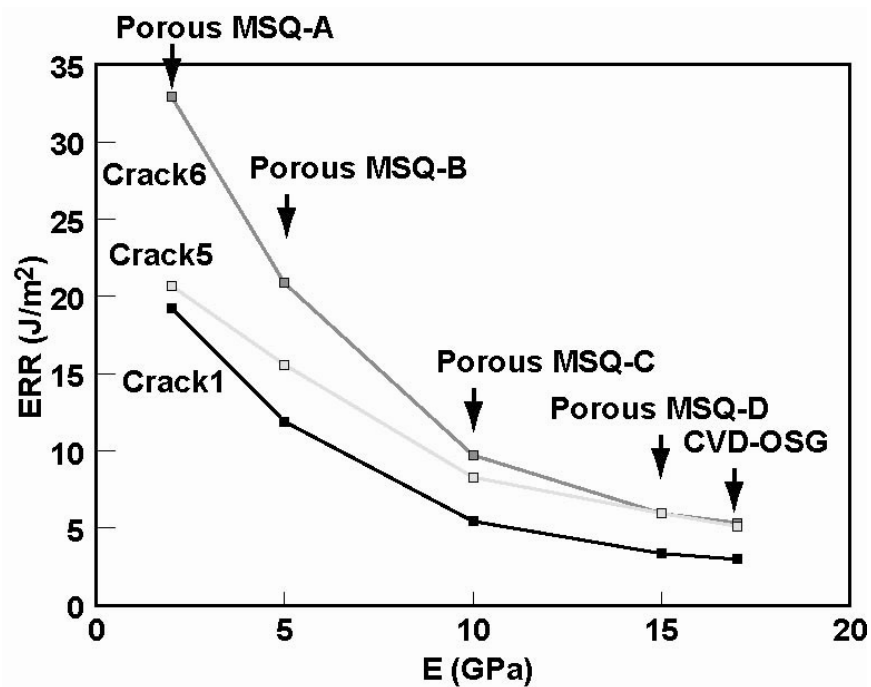


Fig. 5.5. Values of ERR as a function of Young's modulus for low k dielectrics

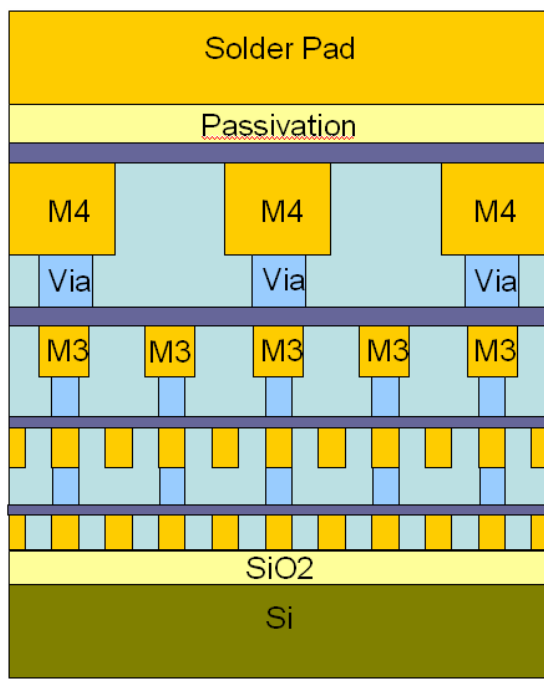
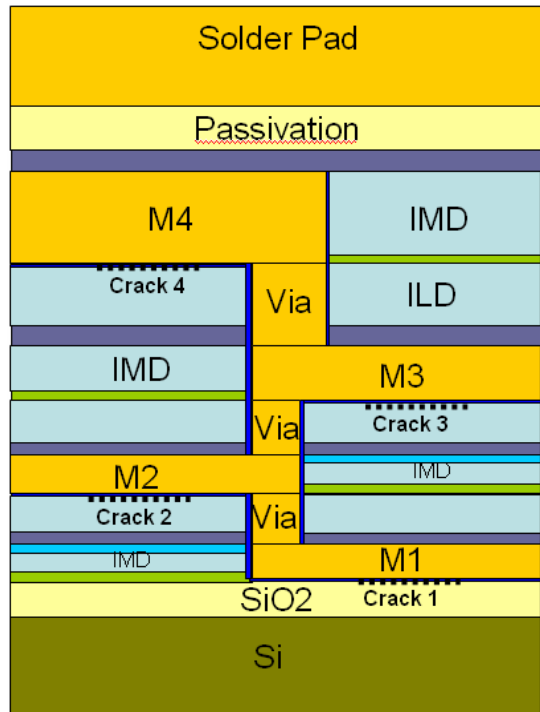


Fig. 6.1. Cross sections of the 3D interconnect model.

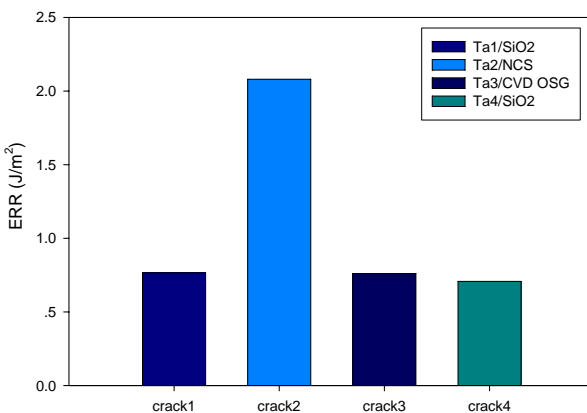
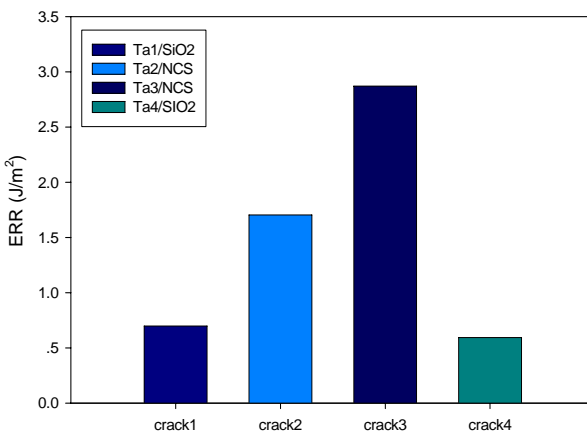
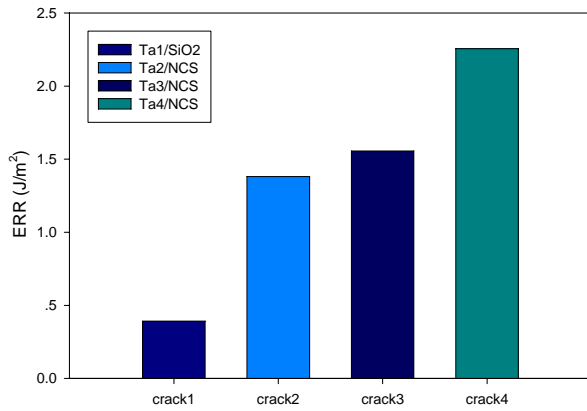


Fig. 6.2. CPI-induced energy release rates for four-level interconnect models with different combinations of interlevel dielectrics: (a) ULK in all levels; (b) SiO_2 in the M4 level and ULK in others, and (c) SiO_2 in M4 and CVD OSG in M3 and ULK in others.

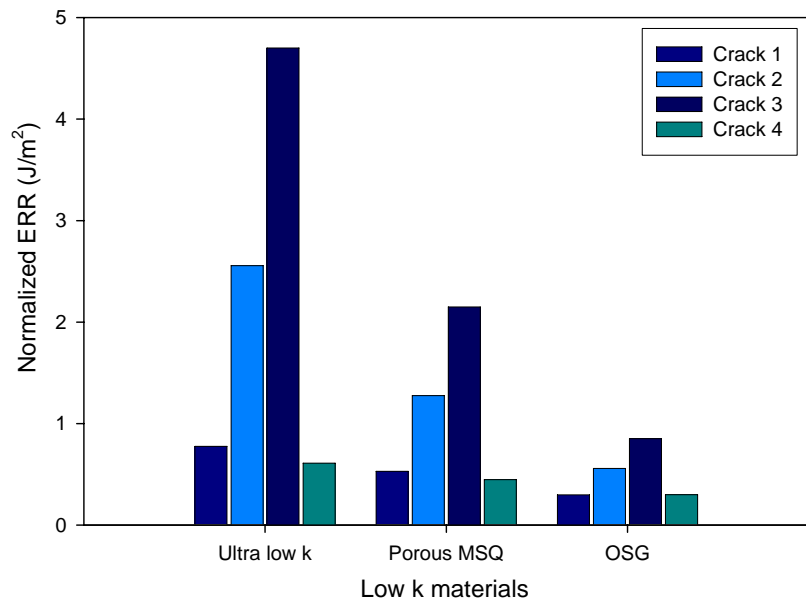


Fig. 6.3. Comparison of CPI-induced energy releases rates in the four-level interconnects with low k and ultralow k ILDs.

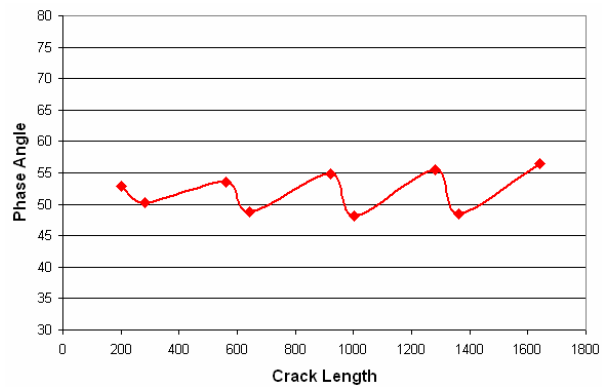
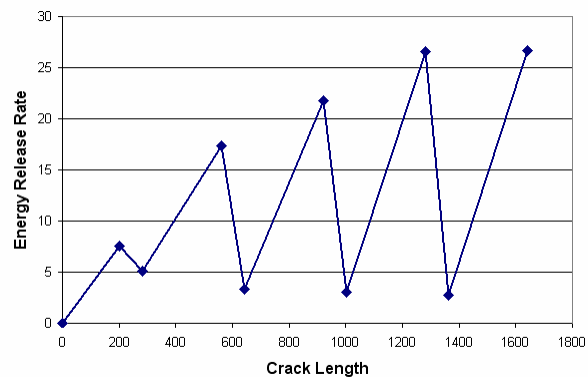
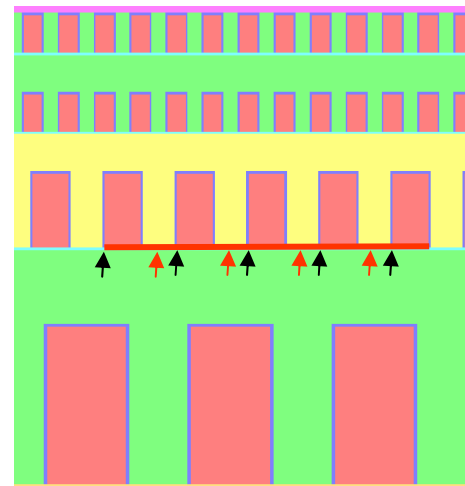


Fig. 6.4. Crack length dependence of the energy release rate and mode mix of an interfacial crack

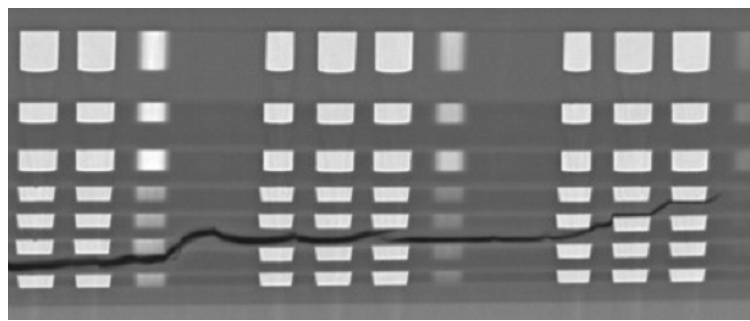


Fig. 6.5. crack propagation in a multilevel interconnect.

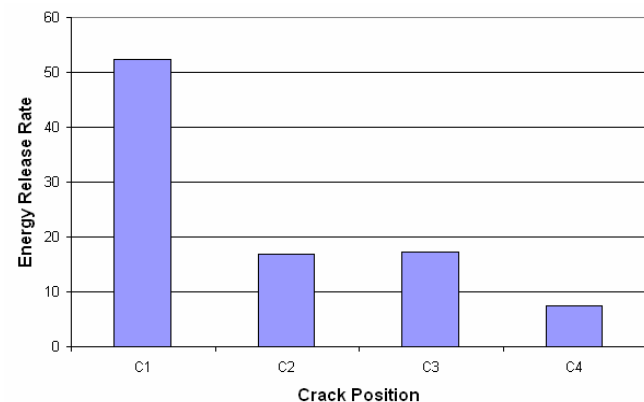
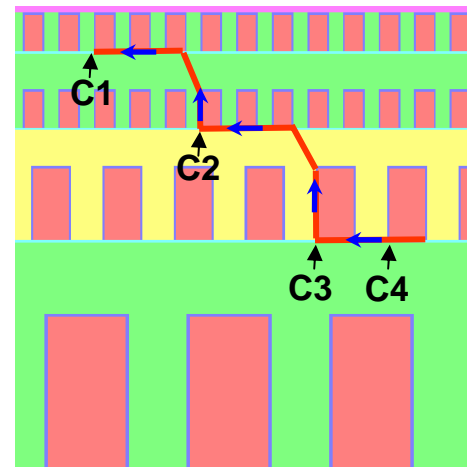


Fig. 6.6. Modeling CPI induced crack propagation in a multilevel interconnect.

References

1. The International Technology Roadmap for Semiconductors 2005 Edition, Semiconductor Industry Association, San Jose, CA.
2. D.C. Edestein, Tech. Dig. IEEE Int. Electron Devices Conf. 1997, pp.773-776.
3. S. Venkaesan, A.V. Gelatos, V. Misra, B. Smith and R. Islam, Tech. Dig. IEEE Int. Electron Devices Conf. 1997, pp.769-772.
4. S. H. Chae, X. F. Zhang, K. H. Lu, H. L. Chao, P. S. Ho, M. Ding, P. Su, T. Uehling, L. N. Ramanathan, J. Materials Science: Materials Electron **18**, 247 (2007).
5. J. K. Shang, Q. L. zeng, L. Zhang and Q. S. Zhu, J. Materials Science: Materials Electron **18**, 211 (2007).
6. P. S. Ho, G.T. Wang, M. Ding, J.H. Zhao and X. Dai, Microelecrtronics Reliability **44**, 719 (2004).
7. Z. Suo, 2003. Reliability of Interconnect Structures, pp. 265-324 in Volume 8: Interfacial and Nanoscale Failure (W. Gerberich, W. Yang, Editors) of Comprehensive Structural Integrity (I. Milne, R.O. Ritchie, B. Karihaloo, Editors-in-Chief), Elsevier, Amsterdam.
8. T. Y. Wu, Y. Tsukada and W. T. Chen, Proc. Electronic Comp. Technology Conf. 1996, p.524.
9. X. Dai, C. Kim, R. Willecke and P. S. Ho, Electronic Packaging Materials Science IX. Materials Res. Soc. Symposium Proc. Vol.445 (1996), p.167.

10. M.R. Miller, I. Mohammed, X. Dai, N. Jiang and P. S. Ho, Proc. Electronic Components and Technology Conf. (1996), p. 979-86.
11. Y. Du, G. T. Wang, C. Merill and P. S. Ho, Proc. Electronic Components and Technology Conf. (1996), pp. 859–64.
12. T. Scherban, G. Xu, C. Merrill, C. Litteken and B. Sun in “Stress-Induced Phenomena in Metallization” AIP Conference Proc. Vol. 817, edited by E. Zschech, K. Maex, P. S. Ho, H. Kawasaki and T. Nakamura (2006).
13. J. Rim, F. Shi, D. Lee, R. Dauskardt, T. Scherban, F. Ohta, K. Abe and S. Jain, to be published.
14. L. Mercado, C. Goldberg, S.-M. Kuo, International Interconnect Technology Conference, 2002. pp 119- 121
15. L. Mercado, S.-M. Kuo, C. Goldberg, and D. Frear, IEEE Transaction on Advanced Packaging, **26**, NOVEMBER 2003
16. G.T. Wang, C. Merrill, J.H. Zhao, S. Groothuis and P. Ho, 2003. Packaging effects on reliability of Cu/low k interconnects. IEEE Trans Device and Materials Reliability, **3**, 119-128.
17. J. H. Zhao, B. Wilkerson and T Uehling, “Stress-Induced Phenomena in Metallization, 7th International Workshop, edited by P.S. Ho, S.P. Baker, T. Nakamura and C.A. Volkert, AIP Conf. Proc. Vol. 714, 2004. pp 52-61.

18. W. Landers, D. Edelstein, L. Clevenger, Proc International Interconnect Technology Conference (2004).
19. G. Wang, P. S. Ho and S. Groothuis, Microelectronics Reliability, **45**, 1079 (2005).
20. C. J. Zhai, U. Ozkan, A. Dubey, Sidharth, R. C. Blish and R. N. Master, Proc. Electronic Components and Technology Conf. (2006), pp. 709-717.
21. C. J. UCHIBORI; X. Zhang, P. S. Ho and T. Nakamura, International Interconnect Technology Conference, 2006.
22. C. J. UCHIBORI; X. Zhang, S. Im, P. S. Ho and T. Nakamura, "Investigation of Mechanical reliability of Cu/low-k multi-layer interconnects in Flip Chip Package", Proc. EUROSime Conference, 2006
23. X. H. Liu, T. M. Shaw, M. W. Lane, E. G. Liniger, B. W. Herbst, D. L. Questad, Chip-package interaction modeling of ultra low-k/copper back end of line. International Interconnect Technology Conference, 2007.
24. D. Post, D. B. Han, P. Ifju. "High Sensitivity Moiré: Experimental Analysis for Mechanics and Materials". New York- Berlin: Springer-Verlag; 1994.
25. Y. Guo, C. K. Lim, W. T. Chen and C. G. Woychik, IBM J. Research Development, **37**, 635 (1993).
26. J.W. Hutchinson and Z. Suo, 1992. Mixed-mode cracking in layered materials. Advances in Applied Mechanics 29, 63-191.

27. Q. Ma, J. Xie, S. Chao, S. El-Mansy, R. McFadden, H. Fujimoto, 1998. Channel cracking technique for toughness measurement of brittle dielectric thin films on silicon substrates. Mater. Res. Soc. Symp. Proc. 516, 331-336.
28. A. A. Volinsky, N. R. Moody, W. W. Gerberich, 2002. Interfacial toughness measurements for thin films on substrates. Acta Materialia 50, 441-466.
29. S.-Y. Kook, R. H. Dauskardt, 2002. Moisture-assisted subcritical debonding of a polymer/metal interface. J. Appl. Phys., 91, 1293–1303.
30. Q. Ma, 1997. A four-point bending technique for studying subcritical crack growth in thin films and at interfaces. J. Mater. Res. 12, 840-845.
31. R. H. Dauskardt, M. Lane, Q. Ma, N. Krishna, 1998. Adhesion and debonding of multi-layer thin film structures. Eng. Fract. Mech., 61, 141–162.
32. Z. Suo, J. W. Hutchinson, 1989. Sandwich specimens for measuring interface crack toughness. Mater. Sci. Eng., A107, 135–143.
33. K. M. Liechti, T. Freda, 1989. On the use of laminated beams for the determination of pure and mixed-mode fracture properties of structural adhesives. Journal of Adhesion, 28, 145-169.
34. G. Fernlund, J. K. Spelt, 1994. Mixed-mode fracture characterization of adhesive joints. Composites Science and Technology 50, 441-449.

35. A. G. Evans, M. Ruhle, B. J. Dalgleish, P. G. Charalambides, 1990. The fracture energy of bimaterial interfaces. *Mater. Sci. Eng. A* 126, 53-64.
36. M. Lane, 2003. Interface fracture. *Annu. Rev. Mater. Res.* 33, 29-54.
37. M. Lane, R. H. Dauskardt, A. Vainchtein, H. Gao, 2000. Plasticity contributions to interface adhesion in thin film interconnect structures. *J. Mater. Res.*, 15, 2758–2769.
38. J. W. Hutchinson, A. G. Evans, 2000. Mechanics of materials: top-down approaches to fracture. *Acta Mater.*, 48, 125–135.
39. M. W. Lane, R. H. Dauskardt, N. Krishna, I. Hashim, 2000. Adhesion and reliability of copper interconnects with Ta and TaN barrier layers. *J. Mater. Res.* 15, 203-211.
40. M. W. Lane, E. G. Liniger, and J. R. Lloyd, 2003. Relationship between interfacial adhesion and electromigration in Cu metallization. *J. Appl. Phys.* **93**, 1417-1421.
41. J. R. Lloyd, M. W. Lane, E. G. Liniger, C. K. Hu, T. M. Shaw, R. Rosenberg, 2005. Electromigration and adhesion. *IEEE Trans. Device and Materials Reliability* 5, 113-118.
42. T. M. Shaw, E. Liniger, G. Bonilla, J. P. Doyle, B. Herbst, X. H. Liu, M. W. Lane, Experimental determination of the toughness of crack stop structures. *IEEE International Interconnect Technology Conference* (2007).
43. R. F. Cook, E. G. Liniger, 1999. Stress-corrosion cracking of low-dielectric-constant spin-on-glass thin films. *J. Electrochemical Soc.* 146, 4439-4448.
44. X. H. Liu, M. W. Lane, T. M. Shaw, E. G. Liniger, R. R. Rosenberg, and D. C. Edelstein,

2004. Low-k BEOL Mechanical Modeling. Proc. Advanced Metallization Conference 2004, pp. 361-367.
45. T. Y. Tsui, A. J. McKerrow, and J. J. Vlassak, 2005. Constraint effects on thin film channel cracking behavior. *J. Mater. Res.* 20, 2266-2273.
46. X. H. Liu, M. W. Lane, T. M. Shaw, E. Simonyi, 2007. Delamination in patterned films. *Int. J. Solids Struct.* 44 (6): 1706-1718.
47. T. Y. Tsui, A. J. McKerrow, J. J. Vlassak, 2006. The effect of water diffusion on the adhesion of organosilicate glass film stacks. *J. Mech. Phys. Solids* 54, 887-903.
48. J. He, G. Xu, Z. Suo, 2004. Experimental determination of crack driving forces in integrated structures. Proc. 7th Int. Workshop on Stress-Induced Phenomena in Metallization, edited by P.S. Ho, S.P. Baker, T. Nakamura, C.A. Volkert, American Institute of Physics, New York, pp. 3-14.
49. J. L. Beuth, 1992. Cracking of thin bonded films in residual tension. *Int. J. Solids Struct.* 29, 63-191.
50. R. Huang, J.H. Prevost, Z.Y. Huang, and Z. Suo, 2003. Channel cracking of thin films with the extended finite element method. *Eng. Frac. Mech.* 70, 2513-2526.
51. T. Nakamura, S. M. Kamath, 1992. Three-dimensional effects in thin-film fracture mechanics. *Mech. Mater.* 13, 67-77.

52. J. M. Ambrico, M. R. Begley, 2002. The role of initial flaw size, elastic compliance and plasticity in channel cracking of thin films. *Thin Solid Films* 419, 144-153.
53. T. Ye, Z. Suo, and A.G. Evans, 1992. Thin film cracking and the roles of substrate and interface. *Int. J. Solids Struct.* 29, 2639-2648.
54. Y. Pang, R. Huang, 2007. Influence of Interfacial Delamination on Channel Cracking of Brittle Thin Films. In: Materials, Processes, Integration and Reliability in Advanced Interconnects for Micro- and Nanoelectronics, edited by Q. Lin, E.T. Ryan, W-L. Wu, D.Y. Yoon (Mater. Res. Soc. Symp. Proc. Vol. 990, Warrendale, PA), B06-04.
55. M. S. Hu, A. G. Evans, 1989. The cracking and decohesion of thin films on ductile substrates. *Acta Metall.* 37, 917-925.
56. J. L. Beuth, N. W. Klingbeil, 1996. Cracking of thin films bonded to elastic-plastic substrates. *J. Mech. Phys. Solids* 44, 1411-1428.
57. R. Huang, J.H. Prevost, and Z. Suo, 2002. Loss of constraint on fracture in thin film structures due to creep. *Acta Materialia* 50, 4137-4148.
58. Z. Suo, J. H. Prevost, J. Liang, 2003. Kinetics of crack initiation and growth in organic-containing integrated structures. *J. Mech. Phys. Solids* 51, 2169-2190.
59. J. Liang, R. Huang, J.H. Prevost, Z. Suo, 2003. Thin film cracking modulated by underlayer creep. *Experimental Mechanics*, 43, 269-279.

60. J. Liang, Z. Zhang, J. H. Prevost, Z. Suo, 2004. Time-dependent crack behavior in an integrated structure. *Int. J. Fracture* **125**, 335-348.
61. M. Huang, Z. Suo, Q. Ma, H. Fujimoto, 2000. Thin film cracking and ratcheting caused by temperature cycling. *J. Mater. Res.* **15**, 1239-1242.
62. M. Huang, Z. Suo, Q. Ma, 2002. Plastic ratcheting induced cracks in thin film structures. *J. Mech. Phys. Solids* **50**, 1079-1098.
63. M. L. Williams, 1959. The stress around a fault or crack in dissimilar media. *Bull. Seismol. Soc. Am.* **49**, 199-204.
64. J. R. Rice, 1988. Elastic fracture mechanics concepts for interfacial cracks. *J. Appl. Mech.* **55**, 98-103.
65. Z. Suo, J. W. Hutchinson, 1990. Interface crack between two elastic layers. *Int. J. Fracture*, **43**, 1-18.
66. H. H. Yu, M. Y. He, J. W. Hutchinson, 2001. Edge effects in thin film delamination. *Acta Mater.* **49**, 93-107.
67. M.Y. He, J.W. Hutchinson, 1989. Crack deflection at an interface between dissimilar elastic materials. *Int. J. Solids Struct.* **25**: 1053-1067.
68. R. J. Farris, C. L. Bauer, 1988. A self-determination method of measuring the surface energy of adhesion of coatings. *J. Adhesion* **26**, 293-300.

69. H. M. Jensen, J. W. Hutchinson, K.-S. Kim, 1990. Decohesion of a cut prestressed film on a substrate. *Int. J. Solids Struct.* 26, 1099-1114.
70. H. F. Nied, 2003. Mechanics of interface fracture with applications in electronic packaging. *IEEE Transactions on Device and Materials Reliability* 3, 129-143.
71. M. W. Lane, X. H. Liu, T. M. Shaw, 2004. Environmental effects on cracking and delamination of dielectric films. *IEEE Trans. Device Mater. Reliability* 4, 142-147.
72. J. J. Vlassak, Y. Lin, T. Y. Tsui, 2005. Fracture of organosilicate glass thin films: environmental effects. *Mater. Sci. Eng. A* 391, 159-174.
73. S. H. Rhee, Y. Du and P. S. Ho, *Journal of Applied Physics* **93**, 3926 (2003).
74. G. T. Wang, D. W. Gan, S. Groothuis and P. S. Ho, *Proc. Electronic Components Technology Conf.* (2006).
75. D. W. Gan, S. Yoon and P. S. Ho, "Effects of Passivation Layer on Stress Relaxation in Cu Line Structures," *IEEE International Interconnect Technology Conference*, (2003),
76. ANSYS Advanced Guide Manual, chapter 9, in ANSYS Version 9.0 Documentation, ANSYS, Inc., 2006.
77. C. F. Shih, R. J. Asaro, 1988. Elastic-plastic analysis of cracks on bimaterial interfaces: Part I-small scale yielding. *J. Appl. Mech.* 55, 299-316.
78. T. Nakamura, 1991. Three-dimensional stress fields of elastic interface cracks. *J. Appl. Mech.* 58, 939-946.

79. M. R. Begley, J. M. Ambrico, 2001. Delamination of thin films from two-dimensional interface flaws at corners and edges. *Int. J. Fracture* 112, 205-222.
80. ABAQUS Theory Manual, Section 2.16, in ABAQUS Version 6.6 Documentation, ABAQUS, Inc., 2006.
81. T. J. R. Hughes, M. Stern, 1980. Techniques for developing special finite element shape functions with particular references to singularities. *Int. J. Numerical Methods in Engineering* 15, 733-751.
82. N. Sukumar, Z. Huang, J.-H. Prevost, Z. Suo, 2004. Partition of unity enrichment for bimaterial interface cracks. *Int. J. Numerical Methods in Engineering* 59, 1075-1102.
83. A. O. Ayhan, H. F. Nied, 1999. Finite element analysis of interface cracking in semiconductor packages. *IEEE Trans. Components and Packaging Technology* 22, 503-511.
84. A. O. Ayhan, A. C. Kaya, H. F. Nied, 2006. Analysis of three-dimensional interface cracks using enriched finite elements. *Int. J. Fracture* 142, 255-276.
85. F. G. Bucholz, R. Sistla, T. Krishnamurthy, 1988. 2D and 3D applications of the improved and generalized Modified Crack Closure Integral Method. In: Computational Mechanics'88 (Atluri SN and Yagawa G, editors), Springer-Verlag, New York.
86. E. F. Rybicki, M. F. Kanninen, 1977. A finite element calculation of stress intensity factors by a modified crack closure integral. *Eng. Frac. Mech.* 9, 931-938.

87. K. N. Shivakumar, P. W. Tan, J. C. Newman Jr., 1988. A virtual crack-closure technique for calculating stress intensity factors for cracked three-dimensional bodies. *Int. J. Fracture* 36, R43-50.
88. R. Krueger, 2002. The virtual crack closure technique: history, approach and applications. NASA/CR-2002-211628.
89. C. T. Sun, C. J. Jih, 1987. On strain energy release rates for interfacial cracks in bimaterial media. *Eng. Frac. Mech.* 28, 13-20.
90. I. S. Raju, J. H. Crews, M. A. Aminpour, 1988. Convergence of strain energy release rate components for edge delaminated composite materials. *Eng. Frac. Mech.* 30, 383-396.
91. T. W. Chow, S. N. Atluri, 1995. Finite element calculation of stress intensity factors for interfacial crack using virtual crack closure integral. *Comput Mech* 16, 417-425.
92. A. Agrawal, A. M. Karlsson, 2006. Obtaining mode mixity for a bimaterial interface crack using the virtual crack closure technique. *Int. J. Fracture* 141, 75-98.
93. G. T. Wang, Ph.D. Thesis, The University of Texas at Austin, 2004.